

# Sub-MHz AC magnetometry with a double-dressed spin qubit in diamond

Kihwan Kim<sup>1</sup>, Yisoo Na<sup>1</sup>, Jungbae Yoon<sup>1</sup>, Dongkwon Lee<sup>1</sup>, Hee Seong Kang<sup>2</sup>, Chul-Ho Lee<sup>2,3,4</sup>, and Donghun Lee<sup>1</sup>

<sup>1</sup> Department of Physics, Korea University, Seoul, 02841, Republic of Korea

<sup>2</sup> KU-KIST Graduate School of Converging Science and Technology, Korea University, Seoul, 02841, Republic of Korea

<sup>3</sup>Department of Integrative Energy Engineering, Korea University, Seoul, 02841, Republic of Korea

<sup>4</sup>Advanced Materials Research Division, Korea Institute of Science and Technology, Seoul, 02792, Republic of Korea

## Abstract

We experimentally demonstrate a protocol that effectively suppresses the qubit–bath interaction in diamond and enables detection of weak AC signals (below 1 MHz) with enhanced signal-to-noise ratio (SNR) up to  $\text{SNR} \approx 17$ . The method is based on AC magnetometry with single- and double-dressed states that are adiabatically transferred from the initial qubit states using concatenated continuous dynamical decoupling. This work paves a way toward sensitive detection of weakly coupled nuclear spins in low-field NMR experiments.

Not all defects in solids are undesirable impurities; some of them turn out to be useful in the field of quantum information [1, 2]. Among these defects, the negatively charged nitrogen-vacancy (NV) center in diamond has been a leading system, particularly of quantum sensing applications, owing to its compatibility with high spatial resolution and high field sensitivity. One of the promising applications is nuclear magnetic resonance (NMR) spectroscopy. Intensive studies on the NV-based NMR have been made using diverse sets of quantum sensing methodologies including pulsed dynamical decoupling (PDD) [3–9], correlation protocols [10–12], quantum memory [13–15], and synchronized readout [16–19]. The pioneering works successfully demonstrate the NMR sensitivity at the single-molecule level [20, 21] and sub-Hz spectral resolution [17–19]. Most of the experiments rely on PDD techniques that provide

prolonged coherence time and enhanced sensitivity, but can be limited in terms of finite pulse widths, pulse errors, and maximum power of the driving field [22, 23]. An alternative approach has been made based on continuous driving of the qubits, called continuous dynamical decoupling (CDD), one representative example being spin locking.

Spin locking is a technique to maintain, or lock, the spin magnetization along a desired location on the Bloch sphere, normally in the transverse plane, by continuously driving (dressing) the qubit. Spin locking was originally introduced in the long history of NMR [24, 25]. For instance, it was implemented to realize the Hartmann–Hahn condition between the spins of different energy scale – e.g., electron spins (GHz) and nuclear spins (MHz) – without use of a large magnetic field [26]. Even in the absence of an external magnetic field, tunable control over the spin’s energy levels is possible by adjusting the amplitude of the driving field. This provides not only selective tuning of the qubit energy over a wide frequency range, but also effective decoupling of the qubit from its noisy environment. Due to its unique advantages, spin locking has been used for both dynamical nuclear polarization (DNP) [26–32] and AC field sensing [33–35] up to hundreds of MHz, beyond the detection bandwidth of typical PDD methods. Recently, a more advanced form of CDD has been using concatenated continuous driving, which introduces a secondary driving field to a qubit [35–39]. This is referred to as the double dressing method as the qubit is dressed twice with two continuous driving fields, and it is expected to provide stronger noise decoupling, and hence enhanced sensitivity, compared to the single dressing method [36–38]. Even if there exist theory proposals and early experimental demonstrations using diamond NV centers, its application for quantum magnetometry has not been studied much.

In this paper, we show that the double dressing method can effectively suppress the interaction between the NV center and its spin bath and, thus, can provide enhanced sensing of sub-MHz magnetic signals. Using the concatenated CDD technique, we adiabatically dress the spin qubit into single- and double-dressed states successively. Ramsey experiment results show that the effective dephasing time is extended by  $\sim 450\%$  for the single-dressed qubit and  $\sim 960\%$  for the double-dressed qubit compared to the bare qubit. We also show selective sensing of AC magnetic field at rf frequency based on the dressed qubits. As the two dressed qubits are orthogonal to each other, one can, in principle, detect rf field with different polarizations (i.e., longitudinal and transverse components enabling vector AC magnetometry). Finally, we demonstrate detection of weak sub-MHz signals with enhanced signal-to-noise ratio (SNR)

using the double dressing method. The spectral broadening and low frequency noise associated with  $^{13}\text{C}$  nuclear spins in diamond are substantially reduced and  $^{13}\text{C}$  Larmor precession frequency is detected with improved SNR ( $\approx 4$ ). In a proof-of-principle experiment, we also do test measurement with weak AC fields of both stochastic and coherent sources at 0.8 MHz. With the double dressing method, we are able to probe the signals with SNR  $\approx 8$  for the stochastic source and SNR  $\approx 17$  for the coherent source. The method introduced in this paper can be applied for low-field NMR and low-frequency AC magnetometry.

The main idea of this paper is illustrated in Fig. 1. By applying two continuous driving fields, we transfer the spin qubit from the bare basis to the single- and double-dressed basis consecutively. For simplicity, we consider a two-level system with the energy splitting of  $\omega_q$ . The bare qubit Hamiltonian can be written as follows:

$$H \approx \frac{\omega_q}{2} \sigma_z + \sigma_z \sum_{\vec{r}} \left[ \frac{A_{\parallel, \vec{r}}}{2} I_{z, \vec{r}} + \frac{A_{\perp, \vec{r}}}{2} I_{x, \vec{r}} \right] + \sum_{\vec{r}} \gamma_{n, \vec{r}} B I_{z, \vec{r}} + \Omega_{\text{MW}} \cos(\omega_{\text{MW}} t) \sigma_x + \Omega_{\text{RF}} \cos(\omega_{\text{RF}} t) \sigma_z \quad (1)$$

, where  $\sigma_x$ ,  $\sigma_y$ ,  $\sigma_z$  are the Pauli matrices,  $I_z$ ,  $I_x$  are the nuclear spin operators with spin 1/2,  $\vec{r}$  is the position vector of each nuclear spin,  $\gamma_{n, \vec{r}}$  is the nuclear spin gyromagnetic ratio,  $B$  is the applied magnetic field, and  $A_{\parallel, \vec{r}}$  and  $A_{\perp, \vec{r}}$  are the parallel and perpendicular hyperfine coupling constants, respectively. We treat  $\hbar$  as 1. The first three terms in eq. 1 denote the qubit energy, the hyperfine interaction between the electron spin and neighboring nuclear spins, and the Zeeman energy of the nuclear spins. The last two terms in eq. 1 correspond to the continuous driving fields (microwave and rf) for the transition to the single- and double-dressed states.  $\Omega_{\text{MW}}$  and  $\omega_{\text{MW}}$ , and  $\Omega_{\text{RF}}$  and  $\omega_{\text{RF}}$ , stand for the amplitude and the frequency of the two driving fields, respectively.

In the large detuning regime of  $\delta_{\text{MW}} = \omega_q - \omega_{\text{MW}} \gg A_{\perp, \vec{r}}$ ,  $A_{\parallel, \vec{r}}$ ,  $\gamma_{n, \vec{r}} B$ , the hyperfine coupling and the nuclear Zeeman terms can be treated as small perturbations and the single-dressed qubit Hamiltonian with the first-order perturbation becomes

$$H_{\text{SD}} \approx \frac{\omega_{\text{SD}}}{2} \sigma_{z, \text{SD}} + \cos(\theta_{\text{SD}}) \sigma_{z, \text{SD}} \sum_{\vec{r}} \left[ \frac{A_{\parallel, \vec{r}}}{2} I_{z, \vec{r}} + \frac{A_{\perp, \vec{r}}}{2} I_{x, \vec{r}} \right] + \sum_{\vec{r}} \gamma_{n, \vec{r}} B I_{z, \vec{r}} + \Omega_{\text{RF}} \cos(\omega_{\text{RF}} t) \sigma_{x, \text{SD}}, \quad (2)$$

where  $\omega_{\text{SD}} = \sqrt{\delta_{\text{MW}}^2 + \Omega_{\text{MW}}^2}$ ,  $\tan(\theta_{\text{SD}}) = \frac{\Omega_{\text{MW}}}{\delta_{\text{MW}}}$ ,  $\sigma_{z, \text{SD}} = \cos(\theta_{\text{SD}}) \sigma_z + \sin(\theta_{\text{SD}}) \sigma_x$ , and  $\sigma_{x, \text{SD}} = \sin(\theta_{\text{SD}}) \sigma_z - \cos(\theta_{\text{SD}}) \sigma_x$ . The hyperfine couplings are suppressed

by a factor of  $\cos(\theta_{\text{SD}}) = \frac{\delta_{\text{MW}}}{\omega_{\text{SD}}}$ . We can do the similar treatment for the double-dressing case.

In the large detuning regime of  $\delta_{\text{RF}} = \omega_{\text{SD}} - \omega_{\text{RF}} \gg \frac{\delta_{\text{MW}}}{\omega_{\text{SD}}} A_{\perp, \vec{r}}, \frac{\delta_{\text{MW}}}{\omega_{\text{SD}}} A_{\parallel, \vec{r}}, \gamma_{n, \vec{r}} B$ , the double-dressed qubit Hamiltonian with the first-order perturbation becomes

$$H_{\text{DD}} \approx \frac{\omega_{\text{DD}}}{2} \sigma_{z, \text{DD}} + \cos(\theta_{\text{SD}}) \cos(\theta_{\text{DD}}) \sigma_{z, \text{DD}} \sum_{\vec{r}} \left[ \frac{A_{\parallel, \vec{r}}}{2} I_{z, \vec{r}} + \frac{A_{\perp, \vec{r}}}{2} I_{x, \vec{r}} \right] + \sum_{\vec{r}} \gamma_{n, \vec{r}} B I_{z, \vec{r}}, \quad (3)$$

where  $\omega_{\text{DD}} = \sqrt{\delta_{\text{RF}}^2 + \Omega_{\text{RF}}^2}$ ,  $\tan(\theta_{\text{DD}}) = \frac{\Omega_{\text{RF}}}{\delta_{\text{RF}}}$ ,  $\sigma_{z, \text{DD}} = \cos(\theta_{\text{DD}}) \sigma_{z, \text{SD}} + \sin(\theta_{\text{DD}}) \sigma_{x, \text{SD}}$ , and  $\sigma_{x, \text{DD}} = \sin(\theta_{\text{DD}}) \sigma_{z, \text{SD}} - \cos(\theta_{\text{DD}}) \sigma_{x, \text{SD}}$ . The hyperfine couplings are decreased even more, by a total factor of  $\cos(\theta_{\text{SD}}) \cos(\theta_{\text{DD}}) = \frac{\delta_{\text{MW}}}{\omega_{\text{SD}}} \frac{\delta_{\text{RF}}}{\omega_{\text{DD}}}$ . The effective suppression of the qubit-bath interaction is the main mechanism to probe target nuclear spins with enhanced SNR, as illustrated in Fig. 1(b).

To see the suppression effect, we first perform electron spin resonance (ESR) and Ramsey interferometry experiments on each qubit of the bare, single-, and double-dressed bases, as shown in Fig. 2. We use the technique of adiabatic passage to coherently map each dressed eigenstate to the corresponding qubit eigenstate [40–43]. As illustrated in Fig. 2(a), we gradually change the amplitude of the continuous driving fields with slow ramping time. In order to do this within the limited time of our qubit decoherence, we introduce a non-zero detuning on purpose to speed up the passage. For instance, we are able to shorten the ramping time by an order of magnitude with a finite detuning, but achieve similar adiabatic state transfer compared to the on-resonant ramping. Note that more detailed discussion on the adiabaticity is available in the supplemental materials.

The upper graphs in Fig. 2(b)-(d) are the ESR results of the qubits with three different bases. The bare qubit frequency at 4007 MHz corresponds to the NV transition between  $m_s = 0$  and  $m_s = +1$  spin states. Here, we apply a  $\sim 400$  G magnetic field to polarize the  $^{15}\text{N}$  nuclear spin into  $m_I = +1/2$  state. The single-dressed qubit is realized at 16.5 MHz, with the continuous drive at  $\Omega_{\text{MW}} = 16$  MHz and  $\omega_{\text{MW}} = 4011$  MHz ( $\delta_{\text{MW}} = 4$  MHz). In a similar manner, the second field at  $\Omega_{\text{RF}} = 2$  MHz and  $\omega_{\text{RF}} = 15$  MHz ( $\delta_{\text{RF}} = -1.5$  MHz) is applied to produce the double-dressed qubit at 2.5 MHz. Through the transitions, the ESR linewidth is noticeably reduced. The effective suppression of the inhomogeneous dephasing is more clearly visible in the Ramsey interferometry measurement, shown in the lower graphs of Fig. 2(b)-(d). The continuous driving can protect the spin from the noisy environment, such as magnetic field

fluctuation; it thus prolongs the inhomogeneous dephasing time  $T_2^*$ . In our measurement,  $T_2^*$  of the dressed qubits are  $3.34 \pm 0.13 \mu\text{s}$  for the single-dressed and  $7.23 \pm 1.18 \mu\text{s}$  for the double-dressed, which are about 4.5 times and 9.6 times longer, respectively, compared to that of the bare qubit,  $0.75 \pm 0.03 \mu\text{s}$ . Note that the oscillations in the Ramsey data are due to non-zero detuning, except for the fast oscillation shown in Fig 2. (d). Its origin is not clear, but we suspect spurious beatings between the rf pulse frequency and the detuning due to imperfect dressing conditions.

Next, we test AC field sensing methods based on the dressed state qubits. The method was first introduced in Ref. [33], but here we extend it to the double-dressed state. We first spin-lock the qubit along the  $x$  axis with a continuous driving of microwave field with an amplitude  $\Omega_{\text{MW}}$ . When we apply a coherent rf field along the  $z$  axis whose frequency,  $\omega_{\text{RF}}$ , matches with the dressed qubit frequency, the spin undergoes a population inversion between  $|+\rangle = \cos\left(\frac{\theta}{2}\right)|1\rangle + \sin\left(\frac{\theta}{2}\right)|0\rangle$  and  $|-\rangle = -\sin\left(\frac{\theta}{2}\right)|1\rangle + \cos\left(\frac{\theta}{2}\right)|0\rangle$ , resulting in a Rabi oscillation of the single-dressed qubit. Figure 3(b) shows an example of the Rabi measurement at a constant  $\omega_{\text{RF}}$  but with different amplitudes  $\Omega_{\text{RF}}$ . From the Rabi frequencies, we are able to obtain the magnitudes of  $\Omega_{\text{RF}}$ . On the other hand, we can sweep the qubit frequency and do spectroscopy measurement, as seen in Fig. 3(c). For instance, we plot the Rabi result at a fixed evolution time of  $\tau = 4 \mu\text{s}$  as a function of  $\Omega_{\text{MW}}$  (i.e., the single-dressed qubit frequency). There exist peaks only when the qubit frequency matches with  $\omega_{\text{RF}}$  and the peak height is proportional to the Rabi frequency,  $\Omega_{\text{RF}}$ . We can repeat the same measurement with the double-dressed qubit. After two consecutive drives of microwave,  $\Omega_{\text{MW}}$ , and rf field,  $\Omega_{\text{RF}}$ , the spin is aligned along the  $z$  axis again. We then apply a third coherent field along the  $x$  axis, whose frequency,  $\omega_{\text{M}}$ , matches that of the double-dressed qubit. Figure 3(d) and (e) are the double-dressed version of the Rabi and the spectroscopy measurements. The amplitude of the third test field,  $\Omega_{\text{M}}$ , is obtained from the Rabi frequency and appears as a peak in the spectroscopy data.

Combination of the coherence protection and the AC field sensing, separately shown in Fig. 2 and Fig. 3, implies that enhanced sensing is possible using the double dressing method. The combined effect becomes more dramatic for the sensing experiments below 1 MHz. As seen in Fig. 3(c) and (e), the noise floor at these frequency ranges is elevated owing to the hyperfine interaction with neighboring  $^{13}\text{C}$  nuclear spins resulting in spectral broadening and low-frequency noise. Due to the large noise background, a high magnetic field is typically required

in the NMR experiment in order to shift the Larmor frequency of target nuclear spins above 1 MHz so that the signal appears against a relatively flat and low-noise background. However, using the double dressing method, we can effectively lower the sub-MHz noise floor by suppressing the hyperfine interaction and the spectral broadening and, thus, can probe target NMR signals without applying a large magnetic field.

The underlying mechanism is illustrated in Fig. 4 (a) with a simple model calculation of the noise spectrum measured by the dressed qubits. For better visualization, we consider only six  $^{13}\text{C}$  nuclear spins whose hyperfine couplings (i.e.,  $A_{\parallel}$  and  $A_{\perp}$ ) are randomly chosen from 0.1 MHz to 1.5 MHz so that the corresponding peaks are broadly spread, from 0.5 MHz to 1.2 MHz, at an external field of  $\sim 400$  G. In the calculated spectrum, we also include  $^1\text{H}$  nuclear spins at 1.7 MHz as an example of the weakly coupled NMR targets. As discussed in eqs. (2)–(3), the hyperfine couplings are suppressed by a factor of  $\sim \frac{\delta_{\text{MW}}}{\omega_{\text{SD}}}$  between the single- and double-dressed qubits. However, even if this factor is consistent for all nuclear spins, the total amount of suppression also depends on the hyperfine couplings – i.e.  $\sim \frac{\delta_{\text{MW}}}{\omega_{\text{SD}}}(A_{\parallel} + A_{\perp})$ ; thus, it differs nuclear spin by nuclear spin. The stronger the hyperfine coupling is, the more the peak shifts in the noise spectrum. In the double-dressed noise spectrum, the peaks of six  $^{13}\text{C}$  nuclear spins shift and converge to  $\sim 0.5$  MHz, which corresponds to the  $^{13}\text{C}$  Larmor frequency at  $\sim 400$  G. As a consequence, the sub-MHz noise floor is reduced and shifted toward lower frequency. On the other hand, the  $^1\text{H}$  NMR peak barely shifts due to the relatively much weaker coupling strength. Combined with the suppressed noise background, this suggests that novel NMR sensing is possible with enhanced SNR.

The simple model calculation explains the measured results in Fig. 3(c) and (e), where the  $^{13}\text{C}$  Larmor peak (marked by a star) stands out against the reduced noise floor. In Fig. 4 (b), we focus on the low-frequency range and repeat the measurement at an increased fixed time of  $\tau = 10 \mu\text{s}$ . The multiple spikes in the single-dressed spectrum, presumably associated with the  $^{13}\text{C}$  spin bath, are shifted and reduced in the double-dressed spectrum, leaving a single dominant peak at around 0.5 MHz, close to the expected location of the  $^{13}\text{C}$  Larmor frequency. Note that  $^1\text{H}$  NMR signal from the water layer on the diamond surface was not observed in this measurement, mainly due to the relatively large depth of the NV centers (e.g.,  $\sim 20$  nm) used in this paper. Instead, we demonstrate detection of weak sub-MHz signal with enhanced SNR using the double dressing method. We applied a test AC field of both coherent and stochastic

signal at 0.8 MHz with 1.2  $\mu\text{T}$  amplitude. Figure 4 (c) shows that the randomly phased stochastic signal is visible in the double-dressed spectrum due to the large amount of suppression in the noise floor (as much as 12 dB). With this measurement, we are able to realize sub-MHz AC sensing with enhanced SNR  $\approx 8$ . Note that the amounts of noise suppression in Fig. 4 (b) and (c) differ from each other mainly due to different NV centers used in the measurements that have dissimilar coherence properties and spin bath environment. The test result with the coherent signal is also shown in the supplemental materials.

In conclusion, we demonstrate suppression of the hyperfine interaction between the NV center and  $^{13}\text{C}$  nuclear spin bath using the concatenated CCD technique. With the help of continuous microwave and rf drives, we adiabatically transfer the NV center into the single- and double-dressed qubits. From the Ramsey experiments, we observe extension of the effective dephasing time,  $T_2^*$ , confirming suppression of the low-frequency noise consisting of the qubit-bath interaction, energy level fluctuation, etc. We also show tunable sensing of rf field based on the dressed state qubits and discuss its potential for novel vector AC magnetometry. Finally, we demonstrate substantial reduction of the low-frequency noise, below  $\sim 1$  MHz, as a result of suppressed spectral broadening and low frequency noise associated with the qubit-bath interaction. In this way, we are able to detect sub-MHz signals with enhanced SNR. This work provides a novel method for probing weakly coupled nuclear spins in the NMR experiment with the diamond NV center, especially with a low magnetic field.

## Acknowledgements

This work is supported by the National Research Foundation of Korea (NRF) grant funded by the Korea government (MSIT) (NRF-2019M3E4A1080232, NRF-2018M3C7A1024602, and NRF-2021R1F1A1049355) and the MSIT(Ministry of Science and ICT), Korea, under the ITRC(Information Technology Research Center) support program (IITP-2022-2020-0-01606) supervised by the IITP(Institute of Information & Communications Technology Planning & Evaluation).

## References

- [1] I. Aharonovich, D. Englund and M. Toth, Solid-state single-photon emitters, Nat. Photon.

10, 631 (2016).

[2] M. Atatüre, D. Englund, N. Vamivakas, S.-Y. Lee, and J. Wrachtrup, Material platforms for spin-based photonic quantum technologies, *Nat. Rev. Mater.* 3, 38 (2018).

[3] T. H. Taminiau, J. J. T. Wagenaar, T. van der Sar, F. Jelezko, V. V. Dobrovitski, and R. Hanson, Detection and control of individual nuclear spins using a weakly coupled electron spin, *Phys. Rev. Lett.* 109, 137602 (2012).

[4] S. Kolkowitz, Q. P. Unterreithmeier, S. D. Bennett, and M. D. Lukin, Sensing distant nuclear spins with a single electron spin, *Phys. Rev. Lett.* 109, 137601 (2012).

[5] N. Zhao, J. Honert, B. Schmid, M. Klas, J. Isoya, M. Markham, D. Twitchen, F. Jelezko, R.-B. Liu, H. Fedder, and J. Wrachtrup, Sensing single remote nuclear spins, *Nat. Nanotechnol.* 7, 657 (2012).

[6] T. Staudacher, F. Shi, S. Pezzagna, J. Meijer, J. Du, C. A. Meriles, F. Reinhard, and J. Wrachtrup, Nuclear magnetic resonance spectroscopy on a (5-nanometer)<sup>3</sup> sample volume, *Science* 339, 561 (2013).

[7] H. J. Mamin, M. Kim, M. H. Sherwood, C. T. Rettner, K. Ohno, D. D. Awschalom, and D. Rugar, Nanoscale nuclear magnetic resonance with a nitrogen-vacancy spin sensor, *Science* 339, 557 (2013).

[8] M. Loretz, S. Pezzagna, J. Meijer, and C. L. Degen, Nanoscale nuclear magnetic resonance with a 1.9-nm deep nitrogen-vacancy sensor, *Appl. Phys. Lett.* 104, 033102 (2014).

[9] M. H. Abobeih, J. Cramer, M. A. Bakker, N. Kalb, M. Markham, D. J. Twitchen, and T. H. Taminiau, One second coherence for a single electron spin coupled to a multi-qubit nuclear-spin environment, *Nature Commun.* 9, 2552 (2018).

[10] J. M. Boss, K. Chang, J. Armijo, K. Cujia, T. Rosskopf, J. R. Maze, and C. L. Degen, One- and two-dimensional <sup>6</sup> nuclear magnetic resonance spectroscopy with a diamond quantum sensor, *Phys. Rev. Lett.* 116, 197601 (2016).

[11] T. Staudacher, N. Raatz, S. Pezzagna, J. Meijer, F. Reinhard, C. A. Meriles and J. Wrachtrup, Probing molecular dynamics at the nanoscale via an individual paramagnetic centre, *Nature Commun.* 6, 8527 (2015).

[12] A. Laraoui, F. Dolde, C. Burk, F. Reinhard, J. Wrachtrup, and C. A. Meriles, High-



resolution correlation spectroscopy of  $c\text{-}^{13}$  spins near a nitrogen-vacancy centre in diamond. *Nat. Commun.* 4, 1651 (2013).

[13] M. Pfender, N. Aslam, H. Sumiya, S. Onoda, P. Neumann, J. Isoya, C. A. Meriles, and J. Wrachtrup, Nonvolatile nuclear spin memory enables sensor unlimited nanoscale spectroscopy of small spin clusters, *Nat. Commun.* 8, 834 (2017).

[14] N. Aslam, M. Pfender, P. Neumann, R. Reuter, A. Zappe, F. F. de Oliveira, A. Denisenko, H. Sumiya, S. Onoda, J. Isoya, and J. Wrachtrup, Nanoscale nuclear magnetic resonance with chemical resolution, *Science* 357, 67 (2017).

[15] Tobias Roskopf, Jonathan Zopes, Jens M. Boss and Christian L. Degen, A quantum spectrum analyzer enhanced by a nuclear spin memory, *npj Quantum Information* (2017).

[16] D. R. Glenn, D. B. Bucher, J. Lee, M. D. Lukin, H. Park, and R. L. Walsworth, High-resolution magnetic resonance spectroscopy using a solid-state spin sensor, *Nature* 555, 351 (2018).

[17] J. Smits, J. T. Damron, A. F. M. Pauli Kehayias, N. Mosavian, I. Fescenko, N. Ristoff, A. Laraoui, A. Jarmola, and V. M. Acosta, Two-dimensional nuclear magnetic resonance spectroscopy with a microfluidic diamond quantum sensor, *Sci. Adv.* 5, eaaw7895 (2019).

[18] S. Schmitt, T. Gefen, F. M. Stürner, T. Uden, G. Wolff, C. Müller, J. Scheuer, B. Naydenov, M. Markham, S. Pezzagna, J. Meijer, I. Schwarz, M. Plenio, A. Retzker, L. P. McGuinness, F. Jelezko, Submillihertz magnetic spectroscopy performed with a nanoscale quantum sensor, *Science* 356, 832 (2017).

[19] J. M. Boss, K. S. Cujia, J. Zopes, C. L. Degen, Quantum sensing with arbitrary frequency resolution, *Science* 356, 837 (2017).

[20] I. Lovchinsky, A. O. Sushkov, E. Urbach, N. P. de Leon, S. Choi, K. De Greve, R. Evans, R. Gertner, E. Bersin, C. Müller, L. McGuinness, F. Jelezko, R. L. Walsworth, H. Park, M. D. Lukin, Nuclear magnetic resonance detection and spectroscopy of single proteins using quantum logic, *Science* 351, 836 (2016).

[21] F. Shi, Q. Zhang, P. Wang, H. Sun, J. Wang, X. Rong, M. Chen, C. Ju, F. Reinhard, H. Chen, J. Wrachtrup, J. Wang, and J. Du, Single-protein spin resonance spectroscopy under ambient conditions, *Science* 347, 1135 (2015).

- [22] T. Ishikawa, A. Yoshizawa, Y. Mawatari, S. Kashiwaya and H. Watanabe, Finite-pulse-width effect on quantum sensing for an asynchronous alternating current magnetic field to dynamical decoupling sequences, *AIP Advances* 9, 075013 (2019).
- [23] M. Hirose, C. D. Aiello, and P. Cappellaro, Continuous dynamical decoupling magnetometry, *Phys. Rev. A* 86, 062320 (2012).
- [24] S. R. Hartmann and E. L. Hahn, Nuclear double resonance in the rotating frame, *Phys. Rev.* 128, 2042 (1962).
- [25] C. P. Slichter, *Principles of Magnetic Resonance*, (Springer, Heidelberg, 1996).
- [26] F. Shagieva, S. Zaiser, P. Neumann, D. B. R. Dasari, R. Stöhr, A. Denisenko, R. Reuter, C. A. Meriles, and J. Wrachtrup, Microwave-assisted cross-polarization of nuclear spin ensembles from optically pumped nitrogen vacancy centers in diamond, *Nano Lett.* 18, 3731 (2018).
- [27] J. Scheuer, I. Schwartz, Q. Chen, D. Schulze-Sünninghausen, P. Carl, P. Höfer, A. Retzker, H. Sumiya, J. Isoya, B. Luy, M. B. Plenio, B. Naydenov, and F. Jelezko, Optically induced dynamic nuclear spin polarisation in diamond, *New J. Phys.* 18, 013040 (2016).
- [28] E. C. Reynhardt, and G. L. High, Dynamic nuclear polarization of diamond. II. Nuclear orientation via electron spin-locking, *J. Chem. Phys.* 109, 4100 (1998).
- [29] I. Hung, and Z. Gan, Spin-locking and cross-polarization under magic-angle spinning of uniformly labeled solids, *J. Magn. Reson.* 256, 23 (2015).
- [30] P. London, J. Scheuer, J.-M. Cai, I. Schwarz, A. Retzker, M. B. Plenio, M. Katagiri, T. Teraji, S. Koizumi, J. Isoya, R. Fischer, L. P. McGuinness, B. Naydenov and F. Jelezko, Detecting and Polarizing Nuclear Spins with Double Resonance on a Single Electron Spin, *Phys. Rev. Lett.* 111, 067601 (2013).
- [31] J. Scheuer, I. Schwartz, S. Müller, Q. Chen, I. Dhand, M. B. Plenio, B. Naydenov, and F. Jelezko, Robust techniques for polarization and detection of nuclear spin ensembles, *Phys. Rev. B* 96, 174436 (2017).
- [32] C. Belthangady, N. Bar-Gill, L. M. Pham, K. Arai, D. L. Sage, P. Cappellaro, and R. L. Walsworth, Dressed-state resonant coupling between bright and dark spins in diamond, *Phys. Rev. Lett.* 110, 157601 (2013).
- [33] M. Loretz, T. Rosskopf, and C. L. Degen, Radiofrequency magnetometry using a single

electron spin, *Phys. Rev. Lett.* 110, 017602 (2013).

[34] D. H. Slichter, R. Vijay, S. J. Weber, S. Boutin, M. Boissonneault, J. M. Gambetta, A. Blais, and I. Siddiqi, Measurement-Induced Qubit State Mixing in Circuit QED from Up-Converted Dephasing Noise, *Phys. Rev. Lett.* 109, 153601 (2012).

[35] A. Stark, N. Aharon, T. Unden, D. Louzon, A. Huck, A. Retzker, U. L. Andersen, and F. Jelezko, Narrow-bandwidth sensing of high-frequency fields with continuous dynamical decoupling, *Nat. Commun.* 8, 1105 (2017).

[36] G. Wang, Y.-X. Liu and P. Cappellaro, Coherence protection and decay mechanism in qubit ensembles under concatenated continuous driving, *New J. Phys.* 22, 123045 (2020).

[37] J.-M. Cai, B. Naydenov, R. Pfeiffer, L. P. McGuinness, K. D. Jahnke, F. Jelezko, M. B. Plenio, and A. Retzker, Robust dynamical decoupling with concatenated continuous driving, *New J. Phys.* 14, 113023 (2012).

[38] Jean Teissier, Arne Barfuss and Patrick Maletinsky, Hybrid continuous dynamical decoupling: a photon-phonon doubly dressed spin, *J. Opt.* 19, 044003 (2017).

[39] G. T. Genov, N. Aharon, F. Jelezko and A. Retzker, Mixed dynamical decoupling, *Quantum Sci. Technol.* 4 035010 (2019).

[40] J. Kölbl, A. Barfuss, M. S. Kasperczyk, L. Thiel, A. A. Clerk, H. Ribeiro, and P. Maletinsky, Initialization of single spin dressed states using shortcuts to adiabaticity, *Phys. Rev. Lett.* 122, 090502 (2019).

[41] M. Demirplak and S. A. Rice, Adiabatic population transfer with control fields, *J. Phys. Chem. A* 107, 9937 (2003).

[42] D. Guéry-Odelin, A. Ruschhaupt, A. Kiely, E. Torrontegui, S. Martínez-Garaot, and J. Muga, Shortcuts to adiabaticity: Concepts, methods, and applications, *Rev. Mod. Phys.* 91, 045001 (2019).

[43] K. N. Zlatanov and N. V. Vitanov, Adiabatic generation of arbitrary coherent superpositions of two quantum states: Exact and approximate solutions, *Phys. Rev. A* 96, 013415 (2017).

## Figure Captions

Fig. 1 Illustration of double dressing method (a) Qubit energy level diagrams in terms of the bare, single-, and double-dressed bases. Driven by continuous microwave, the qubit transfers to a single-dressed qubit whose frequency is determined by the amplitude of the microwave field,  $\Omega_{MW}$ . When the frequency,  $\omega_{RF}$ , matches with  $\Omega_{MW}$ , the second rf drive transfers the qubit once more to a double-dressed qubit whose frequency is  $\Omega_{RF}$ , which equals the amplitude of the rf field. (b) Along the transitions to the double-dressed qubit, the hyperfine interaction between the NV center and  $^{13}\text{C}$  nuclear spin bath can be suppressed a lot more than the reduction of the signal from target NMR spins. This enables sensing of weakly coupled nuclear spins with enhanced signal-to-noise ratio (SNR).

Fig. 2 Coherent protection with dressed states (a) Schematics of the measurement sequence used in the double dressing method. From top to bottom: green pulses for initialization and readout of the NV center, blue (red) continuous drive for single (double) dressing of qubits with microwave (rf) field, and orange pulses or continuous drive for additional qubit manipulation or AC sensing field. For the adiabatic transition, the amplitudes of the driving fields are gradually changed. (b)-(d) ESR (upper panels) and Ramsey (lower panels) measurement results for the bare, single-, and double-dressed qubits whose frequencies are about 4007 MHz, 16.5 MHz, and 2.5 MHz, respectively. The inhomogeneous dephasing time  $T_2^*$  obtained from the fit results of the Ramsey data are  $0.75 \pm 0.03 \mu\text{s}$ ,  $3.34 \pm 0.13 \mu\text{s}$ , and  $7.23 \pm 1.18 \mu\text{s}$  respectively. The slow oscillations correspond to the detunings used in the Ramsey measurements. Potential sources for the fast oscillations in (d) are discussed in the main text and the supplemental materials.

Fig. 3 Sensing AC field with dressed states (a) Illustration of the dressed qubit evolution in the Bloch sphere. (b) and (d) Single- and double-dressed versions of the Rabi oscillation. For single (double)-dressed qubit: coherent rf (manipulation) field with  $\sigma_z$  ( $\sigma_x$ ) component drives the transition between  $|+\rangle$  ( $|0\rangle$ ) and  $|-\rangle$  ( $|1\rangle$ ), and the oscillation frequency is proportional to  $\Omega_{RF}$  ( $\Omega_M$ ). (c) and (e) Noise spectrum measured by the single- and double-dressed qubits. The

qubit contrast data in (b) or (d) at fixed evolution times of  $\tau = 4 \mu\text{s}$  and  $\tau = 5 \mu\text{s}$ , respectively, are plotted as a function of the qubit frequency that are tuned by adjusting  $\Omega_{\text{MW}}$  (for single-dressed) or  $\Omega_{\text{RF}}$  (for double-dressed). AC signal appears as a peak only when the qubit frequency matches with the signal frequency, and the peak height is roughly proportional to the magnitude of the Rabi frequency in (b) and (d). The small peak in (e) marked by a star is discussed in Fig. 4.

Fig. 4 Sub-MHz AC magnetometry based on double-dressed qubit (a) Calculated noise spectrum at the low frequency regime for the single-dressed (upper graph) and double-dressed (lower graph) qubits. In this calculation, we consider six  $^{13}\text{C}$  nuclear spins whose hyperfine couplings vary from 0.1 MHz to 1.5 MHz and assume an external field at 400 G. We also include weakly coupled  $^1\text{H}$  nuclear spins as an example of the target NMR spins. Black dotted lines denote low frequency noise other than the spin bath noise. The calculation shows that the widely spread  $^{13}\text{C}$  peaks shift toward a single peak corresponding to the  $^{13}\text{C}$  Larmor frequency due to the suppression of the hyperfine interaction in the double-dressed qubit. In contrast to the spin bath, the  $^1\text{H}$  peak barely moves, suggesting novel NMR sensing of weakly coupled nuclear spins with enhanced SNR. (b) Measured noise spectrum by the single- and double-dressed qubits. Multiple noise spikes in the single-dressed spectrum disappear in the double-dressed spectrum, leaving a single prominent peak whose frequency equals the expected  $^{13}\text{C}$  Larmor frequency. (c) Same measurement as (b) but with a different NV center. In this case, the noise floor is suppressed even more, as much as 12 dB. As a test AC signal, we apply randomly phased stochastic noise at 0.8 MHz with 1.2  $\mu\text{T}$  amplitude and detect it with  $\text{SNR} \approx 8$  in the double-dressed measurement.

Fig. 1

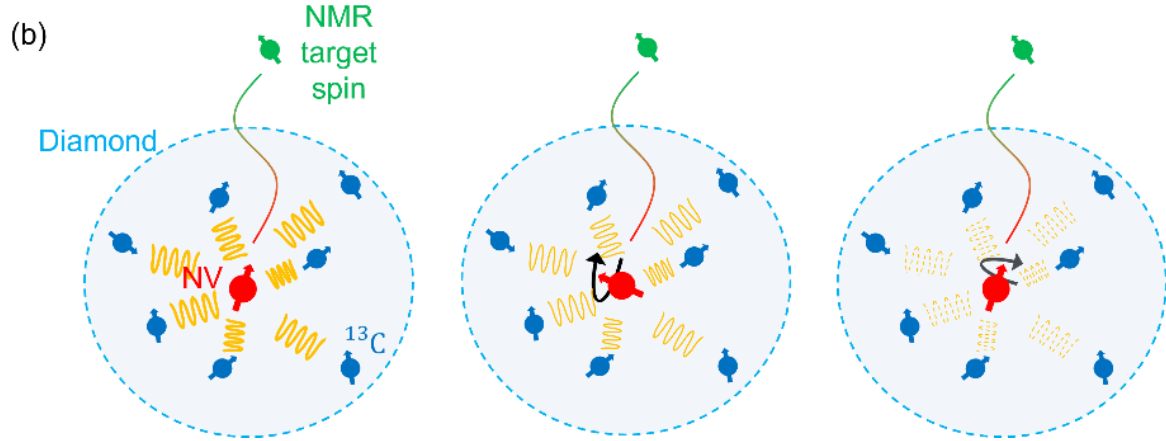
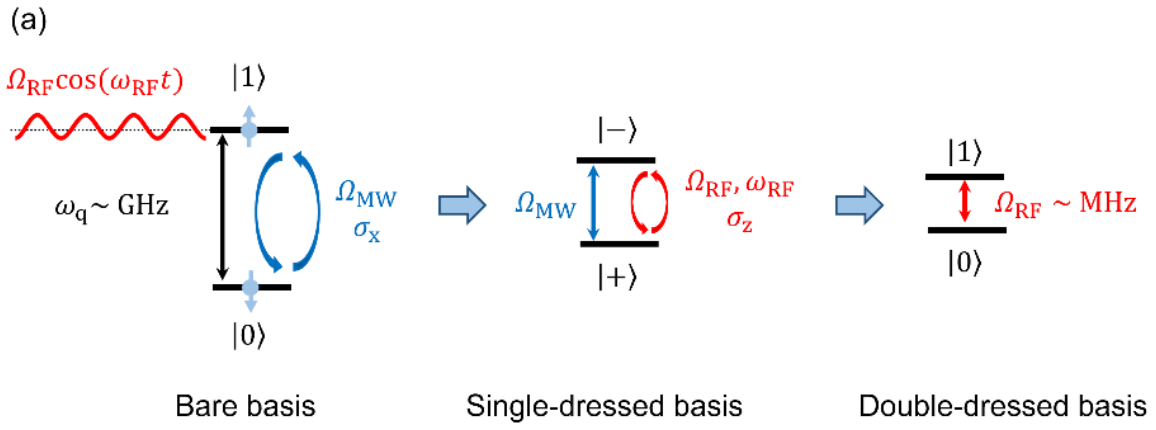
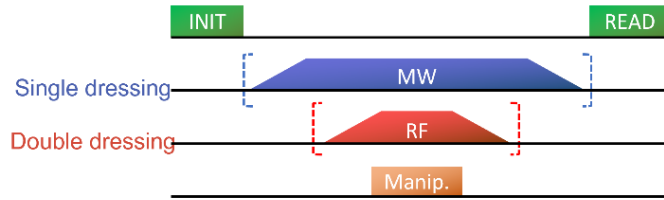


Fig. 2

(a)



(b)

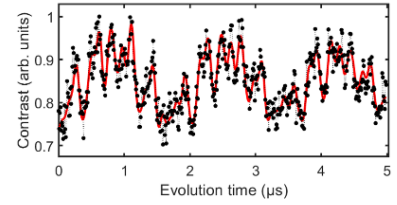
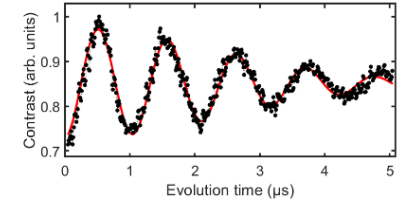
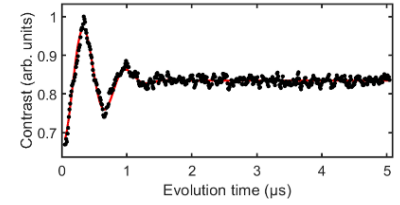
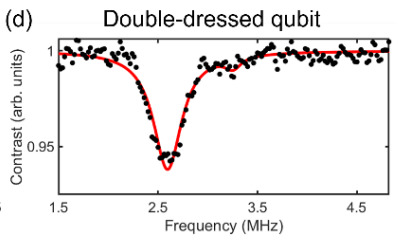
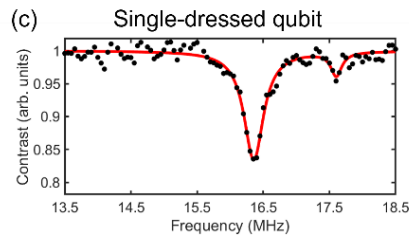
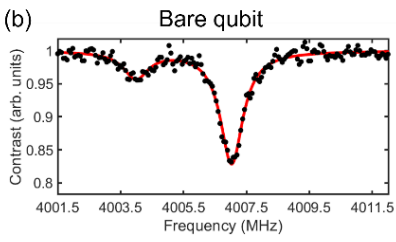


Fig. 3

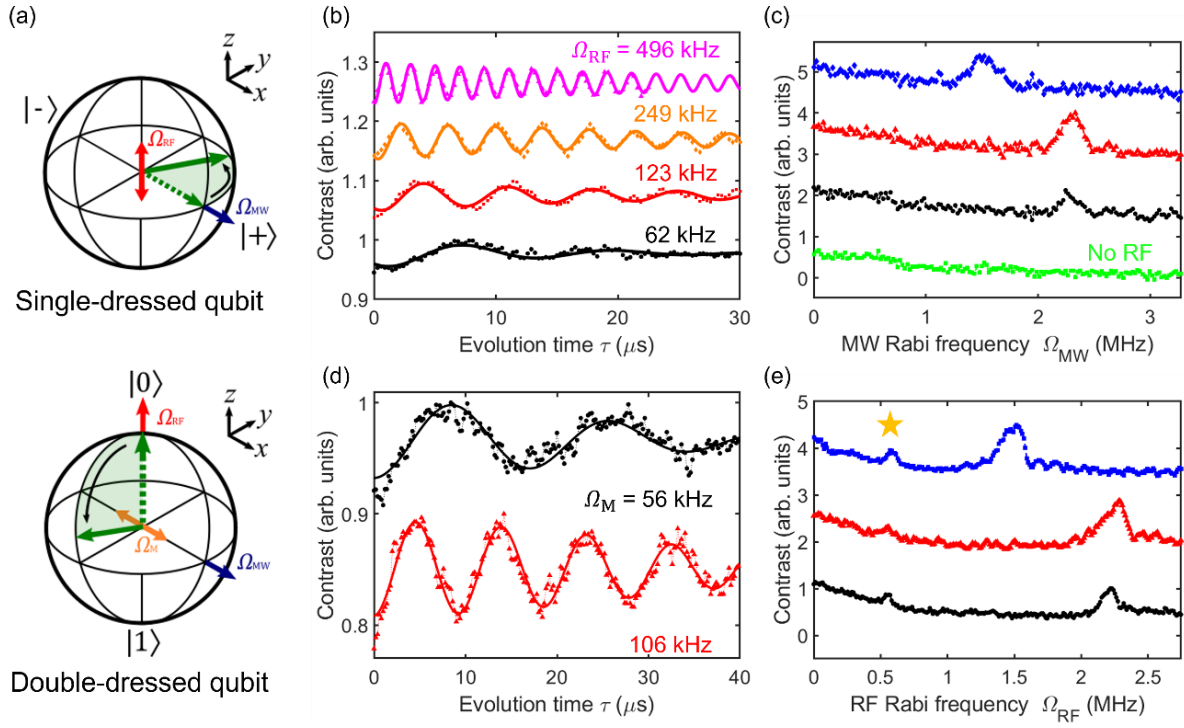
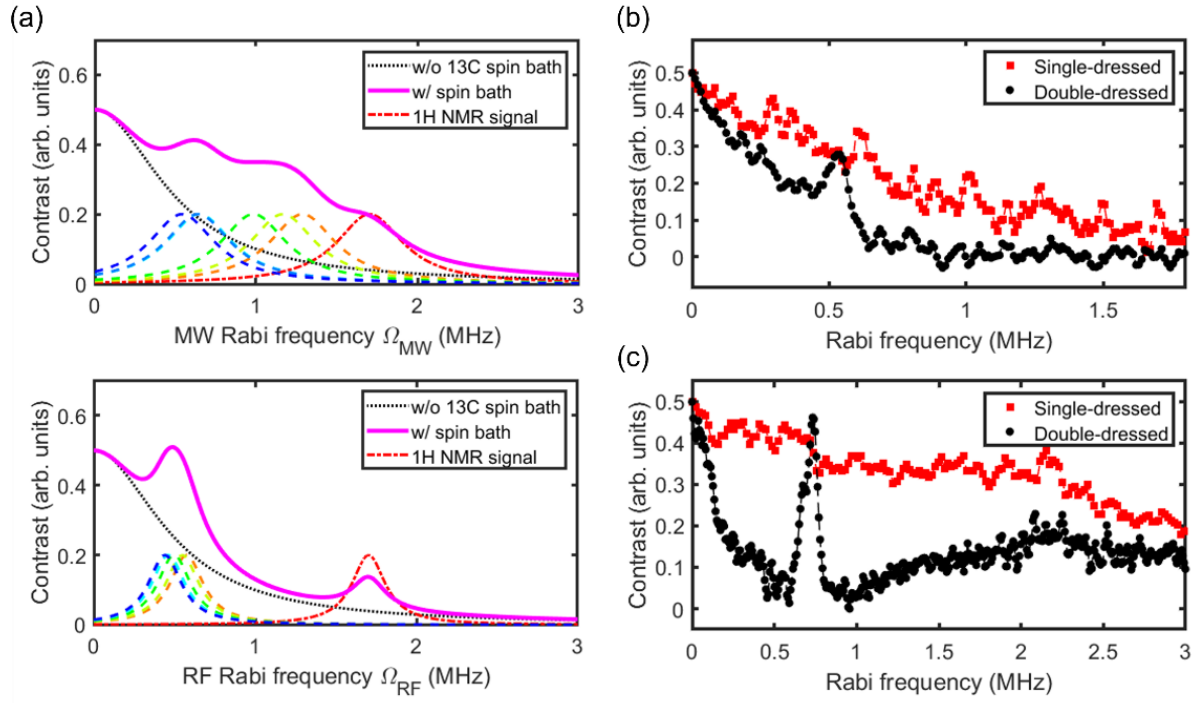




Fig. 4



# Supplemental material: Sub-MHz AC magnetometry with a double-dressed spin qubit in diamond

Kihwan Kim<sup>1</sup>, Yisoo Na<sup>1</sup>, Jungbae Yoon<sup>1</sup>, Dongkwon Lee<sup>1</sup>, Hee Seong Kang<sup>2</sup>, Chul-Ho Lee<sup>2,3,4</sup>, and Donghun Lee<sup>1</sup>

<sup>1</sup> Department of Physics, Korea University, Seoul, 02841, Republic of Korea

<sup>2</sup> KU-KIST Graduate School of Converging Science and Technology, Korea University, Seoul, 02841, Republic of Korea

<sup>3</sup>Department of Integrative Energy Engineering, Korea University, Seoul, 02841, Republic of Korea

<sup>4</sup>Advanced Materials Research Division, Korea Institute of Science and Technology, Seoul, 02792, Republic of Korea

## 1. Diamond sample

A commercial electronic-grade single crystal diamond is used in this paper (Element 6). The sample was implanted with nitrogen ions at 7° tilt angle,  $1 \times 10^9/\text{cm}^2$ , and 15 keV (Innovion) and then Ar annealed at 850 °C for 2 hours to create NV centers. After annealing, the sample was treated with tri-acids for 2 hours and oxygen annealed at 465 °C for 4 hours to make the NV centers' charge state stable.

## 2. Experiment setup

### 2-1 Confocal microscope

A home-built confocal scanning microscope is used to image and readout the diamond NV centers (Fig. S1). 532 nm laser is controlled by an acousto-optic modulator (AOM, IntraAction ATM-200C1) to generate laser pulse. The 532 nm excitation beam and the NV's fluorescence signal of ~ 630 – 800 nm are separated by a dichroic mirror. The fluorescence signal is spatially filtered with a confocal pinhole of 50 μm diameter and then focused to the single photon

detector, avalanche photon detector (APD, Excelitas SPCM-AQRH-14-FC). A band pass filter and a notch filter block reminiscent green laser going in to the APD. The external DC magnetic field is applied by a permanent magnet maneuverable with a 3-axis translation stage.

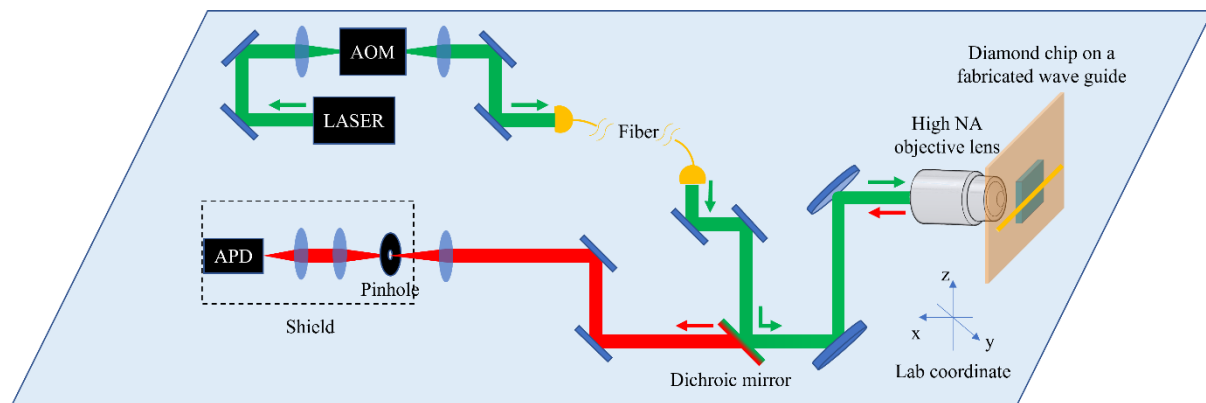


Fig. S1 Schematics of the experiment setup

## 2-2 Microwave and rf control electronics

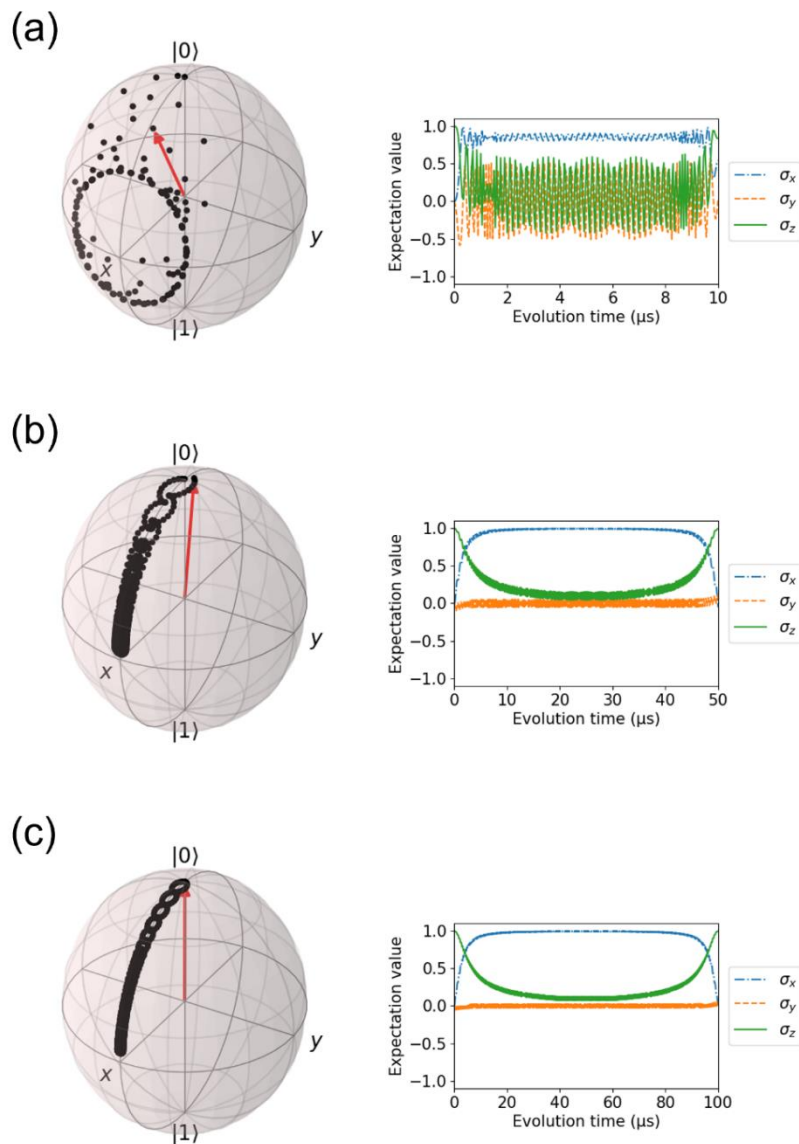
Two Keysight M8190 arbitrary waveform generator (AWG) modules (total 4 channels) with a Keysight M8192 synchronization module generate microwave ( $\sim$  GHz) and rf ( $\sim$  MHz) continuous waves or pulses that are used to control the spin qubit. The control fields are further amplified by microwave or rf amplifiers that are combined by a bias tee to be delivered to the NV centers with a coplanar wave guide (CPW) fabricated on a glass substrate or a bonded gold wire.

## 3. Adiabatic passage

We adiabatically map the dressed qubit state to the bare qubit state so that the coherent control and readout of the qubit state is possible. Previous works have discussed about adiabatic passage and suggested methods to speed up the process [1–4]. For instance, adding a counter-diabatic driving to a resonant driving will speed up the adiabatic process and enhance the process fidelity [2]. However, the technique requires precise design of the phase and amplitude of the control pulse at each time. On the other hand, dressing with a non-zero finite detuning

can be an alternative and a relatively easy way to realize fast adiabatic passage. In this paper, we adopted the latter method. As discussed in Fig. 2(a), we linearly ramp the amplitude of detuned driving fields and gradually transfer the qubit to the target dressed state. As far as the energy along the principal axis is maintained larger than the increasing transverse energy, we can ramp the amplitude faster than the resonant dressing case without losing the adiabaticity.

Fig. S2 QuTiP simulation of adiabatic passage. Spin evolves from  $|0\rangle$  to  $|1\rangle$  with various



ramping time of (a) 2  $\mu\text{s}$ , (b) 20  $\mu\text{s}$ , and (c) 40  $\mu\text{s}$ . Rabi frequency of 15 MHz and detuning of 1.5 MHz are the same for all the cases. The expectation values of the x, y, and z components are plotted together with the Bloch sphere representations.

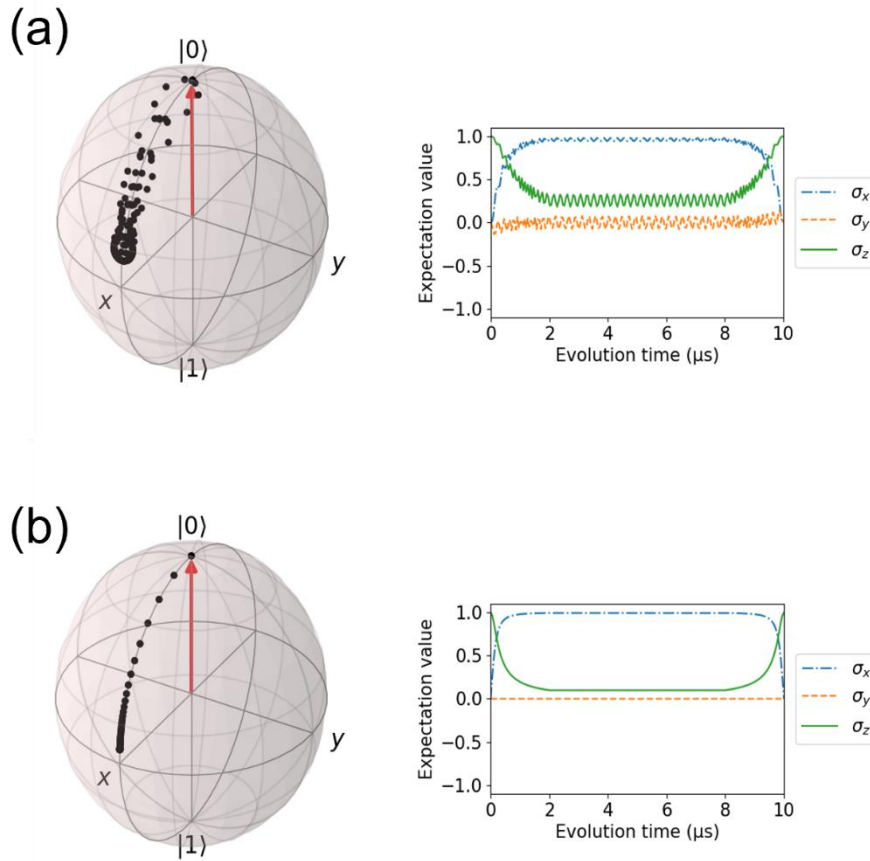


Fig. S3 QuTiP simulation of adiabatic passage. (a) Detuning is increased to 4 MHz compared to Fig. S2(a). Ramping time (2  $\mu\text{s}$ ) and Rabi frequency (15 MHz) are the same as Fig. S2(a). (b) Counter-diabatic driving method. Two drives are used with the same parameters but different axes, i.e.  $x$  for one drive and  $y$  for the other. 2  $\mu\text{s}$  ramping time, 15 MHz Rabi frequency and 1.5 MHz detuning are used.

As the detuning and the ramping time are competing to each other to maintain the adiabaticity, we need to find their optimal parameters. We first do simulation of the qubit evolution with various transfer conditions using an open-source Quantum Toolbox in Python, QuTiP[5, 6]. Figure S2 and S3 are examples of the simulation. Starting from  $|0\rangle$ , the qubit evolves to  $|+\rangle$  and returns back to  $|0\rangle$ . As seen in Fig. S2(a), when the detuning is 1.5 MHz and the Rabi frequency is 15 MHz, 2  $\mu\text{s}$  ramping time is not slow enough to maintain the adiabaticity and the final state fidelity (how much back to the initial state,  $|0\rangle$ ) is 0.919 after total evolution time of 10  $\mu\text{s}$  including two 2  $\mu\text{s}$  ramping time and 6  $\mu\text{s}$  locking time. This can be improved by two different methods. First method is simply increasing the ramping time. Figure S2(b) is

the same process as Fig. S2(a) but with ten times longer ramping time, i.e. 20  $\mu\text{s}$ . The adiabaticity recovers and the final state fidelity becomes 0.999 after total evolution time of 50  $\mu\text{s}$  (two 20  $\mu\text{s}$  ramping time and 10  $\mu\text{s}$  locking time). Another solution is introducing larger detuning, for example 4 MHz, while keeping the ramping time as 2  $\mu\text{s}$ . As shown in Fig. S3(a), high state fidelity comparable to the first method is realized. In this paper, we use the latter method to have the ramping time as short as possible. Note that there exist other adiabatic methods such as using the counter-diabatic driving [2] as shown in Fig. S3(b).

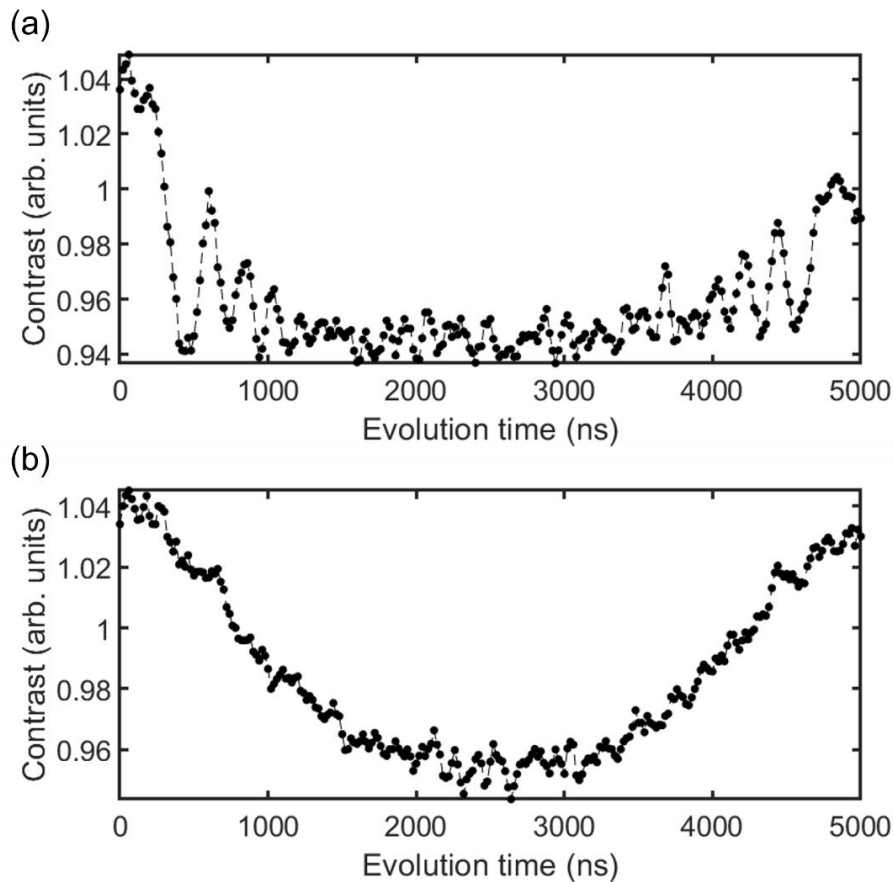


Fig. S4 Testing the adiabatic passage. (a) Resonant ramping, and (b) ramping with 3 MHz detuning. Rabi frequency is 7.5 MHz for both cases.

Figure S4 compares experimental results with two different adiabatic conditions, i.e. resonant ramping and ramping with non-zero detuning. For the former process, the ramping time is not long enough and results in oscillations during the ramping and imperfect recovery to the initial state. On the other hand, the latter process does not involve oscillations and the qubit returns

to the initial state with higher fidelity. Note that due to the non-zero detuning, however, the dressed principal axis is not perfectly orthogonal to the bare basis axis but tilted with a certain angle of  $\theta$  which is determined by the Rabi frequency  $\Omega$  and the detuning  $\delta$  through the relation of  $\tan(\theta) = \frac{\Omega}{\delta}$ . Also note that diabatic evolution can still exist even if we try to adiabatically dress the qubit, especially when the qubit is doubly dressed. The spurious signal in Fig. 2(d) can be explained by this diabatic evolution. The diabatically evolved populations should undergo incoherent dynamics so that there can be additional fast oscillations in the Ramsey interferometry.

#### 4. Pulse sequences for the double dressing method

We briefly explain our qubit control pulse sequence used in Fig. 2(a). In Fig. S5, we visualize the pulse sequence that the AWG makes to realize the double-dressed Ramsey experiment. The frequencies of the applied driving fields in Fig. S5 are not real values used in the experiments but are chosen to enhance the visibility of the waves. The laser pulse controls the AOM for initialization and readout of the NV center. The sampling trigger goes to the data acquisition system (DAQ) which collect the photon count data from the APD.

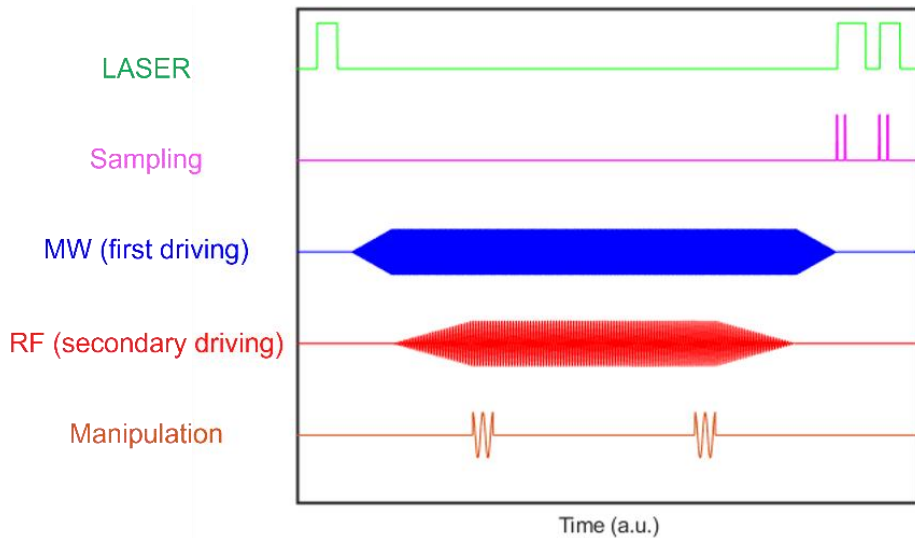


Fig. S5 Pulse sequence used for the double-dressed Ramsey experiment

#### 5. Dressed ESR experiments

Throughout the experiments, an external DC field of  $\sim 400$  G is applied, and the nitrogen nuclear spin is polarized. The ESR experiments in Fig. 2(a) shows that the  $^{15}\text{N}$  nuclear spin is polarized to  $m_I = +1/2$ . Therefore, we ignore the  $^{15}\text{N}$  hyperfine split doublet and treat the electron spin states of  $m_s = +1$  and  $m_s = 0$  as the effective two-level system. Our bare qubit frequency is set to be 4007.4 MHz which is associated with  $m_I = +1/2$  sub-state. When we apply 4 MHz blue-detuned microwave driving with 16 MHz Rabi frequency, the single-dressed qubit energy becomes 16.5 MHz. A similar process occurs for the double-dressed qubit whose frequency becomes 2.5 MHz driven by the 1.5 MHz red-detuned rf driving with 2.0 MHz Rabi frequency.

## 6. ESR linewidth narrowing due to suppression of hyperfine coupling

Here we do a simple toy model calculation for the ESR linewidth narrowing shown in Fig. 2(b)-(d). We assume a hyperfine split doublet consisting of the ESR curve as shown in Fig. S6. In brief, dressing the qubit reduces the hyperfine coupling and thus results in the linewidth narrowing. Given the original electron resonance frequencies of  $f_1$ ,  $f_2$ , Rabi frequency  $\Omega$ , detuning  $\delta$  and the hyperfine splitting of  $A$ , the dressed resonance frequencies become  $\sqrt{\delta^2 + \Omega^2}$  and  $\sqrt{(\delta + A)^2 + \Omega^2}$  (for simplicity, the non-secular terms are ignored). If we assume  $\Omega \gg \delta > A$ , which is an easily fulfilled condition in pure diamond samples as the hyperfine interactions are usually less than 1 MHz [11] while one can easily fulfill the Rabi frequency over 10 MHz, we can write the new energy splitting of  $\sqrt{(\delta + A)^2 + \Omega^2} - \sqrt{\delta^2 + \Omega^2}$  as,

$$\begin{aligned} \sqrt{(\delta + A)^2 + \Omega^2} - \sqrt{\delta^2 + \Omega^2} &= \Omega \left( 1 + \left( \frac{\delta + A}{\Omega} \right)^2 \right)^{\frac{1}{2}} - \Omega \left( 1 + \left( \frac{\delta}{\Omega} \right)^2 \right)^{\frac{1}{2}} \\ &\approx \Omega \left( 1 + \frac{1}{2} \left( \frac{\delta + A}{\Omega} \right)^2 \right) - \Omega \left( 1 + \frac{1}{2} \left( \frac{\delta}{\Omega} \right)^2 \right) = \frac{A^2 + 2A\delta}{2\Omega} \quad (\text{S1}) \end{aligned}$$

, which is about  $\frac{\delta}{\Omega}$  times smaller than the original splitting of  $A$ . Thus, the energy splitting can be easily reduced by more than an order of magnitude in the most cases depending on the magnitude of detuning, which is also easy to be controlled. Figure S7 shows an example plot of the energy splitting versus the Rabi frequency when  $A = 0.3$  MHz and a relatively large detuning of  $\delta = 3$  MHz.



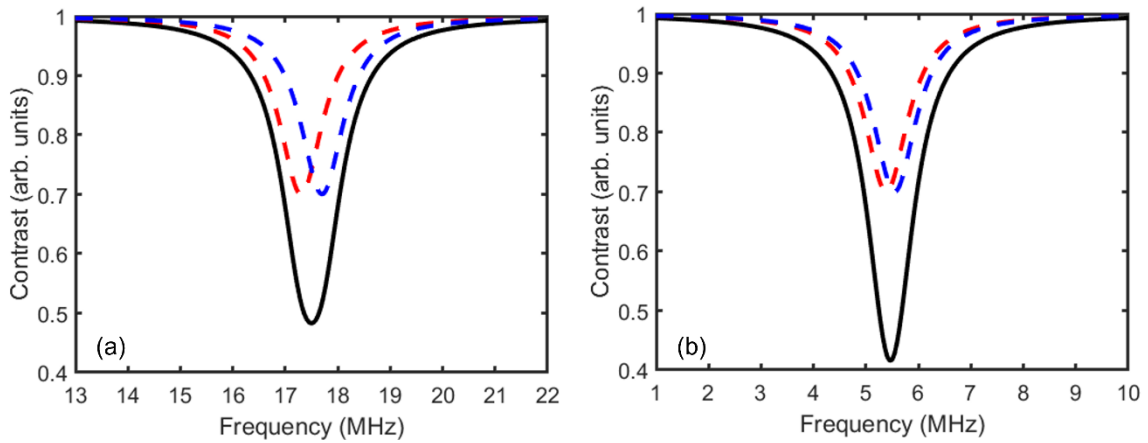


Fig. S6 Dressing reduces ESR linewidth owing to the suppression of hyperfine coupling – a toy model. The two dashed curves correspond to the hyperfine split doublets that form the ESR curve (solid line); (a) and (b) are before and after the dressing field. Upon application of continuous driving (5 MHz Rabi frequency and 2 MHz detuning), the hyperfine splitting is reduced and the ESR linewidth is narrowed by a factor of  $\sim 2/5$ . The intrinsic linewidth are assumed to be 0.3 MHz for both cases.

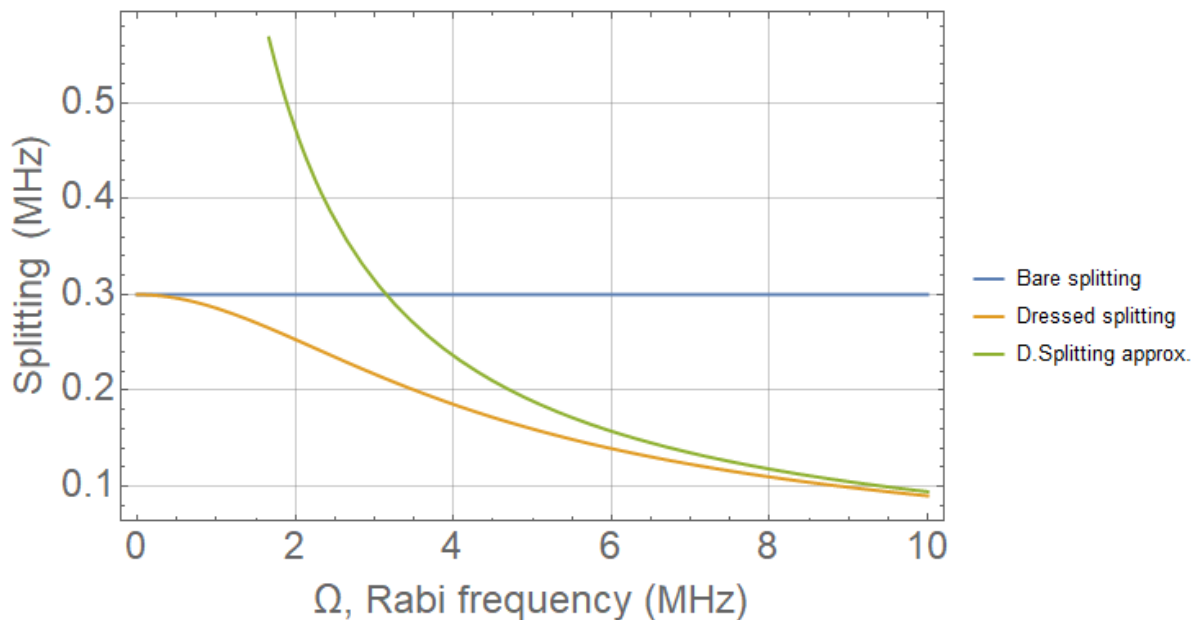


Fig. S7 Comparison of the energy splitting between the bare qubit and single-dressed qubit. The green curve (dressed splitting approximation) is based on eq. S1.  $A = 0.3$  MHz, and  $\delta = 3$  MHz.

## 7. Derivation of the dressed Hamiltonian : resonant cases

Here we derive Hamiltonians for the single- and double-dressed states. For the singly dressing case, the bare qubit Hamiltonian is written with one driving field,

$$H \approx \frac{\omega_q}{2} \sigma_z + \sigma_z \sum_{\vec{r}} \left[ \frac{A_{\parallel\vec{r}}}{2} I_{z,\vec{r}} + \frac{A_{\perp\vec{r}}}{2} I_{x,\vec{r}} \right] + \sum_{\vec{r}} \gamma_{n,\vec{r}} B I_{z,\vec{r}} + \epsilon \sigma_z + \Omega_{\text{MW}} \cos(\omega_{\text{MW}} t) \sigma_x. \quad (\text{S2})$$

In terms of the environmental noise, we consider two terms; hyperfine interaction with the nuclear spin bath and qubit energy fluctuation along the  $z$  axis,  $\epsilon$ . As a dressing field, we consider a continuous microwave drive whose frequency is  $\omega_{\text{MW}}$  and amplitude is  $\Omega_{\text{MW}}$ . Without loss of generality, we consider the field is oscillating along the  $x$  axis. We move to the rotating frame via a unitary transformation  $\hat{U}$ , so that the time dependency to be removed,

$$\hat{U} = e^{i \frac{\omega_{\text{MW}}}{2} t \sigma_x}. \quad (\text{S3})$$

Then after the rotating wave approximation (RWA), the Hamiltonian becomes,

$$H_{\text{SD}} \approx \frac{\delta_{\text{MW}}}{2} \sigma_z + \frac{\Omega_{\text{MW}}}{2} \sigma_x + \sum_{\vec{r}} \left[ \frac{A_{\parallel\vec{r}}}{2} \sigma_z I_{z,\vec{r}} + \frac{A_{\perp\vec{r}}}{2} \sigma_z I_{x,\vec{r}} \right] + \sum_{\vec{r}} \gamma_{n,\vec{r}} B I_{z,\vec{r}} + \epsilon \sigma_z \quad (\text{S4})$$

, where  $\delta_{\text{MW}} = \omega_q - \omega_{\text{MW}}$ . The noise terms maintain their original forms as they commute with  $\sigma_z$ . This can be further simplified by defining a variable  $\theta_{\text{SD}}$  such that  $\tan(\theta_{\text{SD}}) = \frac{\Omega_{\text{MW}}}{\delta_{\text{MW}}}$ .

With the continuous driving, the initial bare qubit eigenbasis  $\{|0\rangle, |1\rangle\}$  along the  $z$  axis is transformed to the new eigenbasis  $\{|+\rangle, |-\rangle\}$ , which is now tilted to some degrees from the  $z$  axis. This is called the dressed basis,

$$\begin{bmatrix} |-\rangle \\ |+\rangle \end{bmatrix} = \begin{bmatrix} -\sin(\frac{\theta_{\text{SD}}}{2}) & \cos(\frac{\theta_{\text{SD}}}{2}) \\ \cos(\frac{\theta_{\text{SD}}}{2}) & \sin(\frac{\theta_{\text{SD}}}{2}) \end{bmatrix} \begin{bmatrix} |1\rangle \\ |0\rangle \end{bmatrix}. \quad (\text{S5})$$

If we consider  $\delta_{\text{MW}} = 0$  for simplicity, the Hamiltonian in eq. S4 becomes

$$H_{\text{SD}} \approx \frac{\Omega_{\text{MW}}}{2} \sigma_x + \sum_{\vec{r}} \left[ \frac{A_{\parallel\vec{r}}}{2} \sigma_z I_{z,\vec{r}} + \frac{A_{\perp\vec{r}}}{2} \sigma_z I_{x,\vec{r}} \right] + \sum_{\vec{r}} \gamma_{n,\vec{r}} B I_{z,\vec{r}} + \epsilon \sigma_z. \quad (\text{S6})$$

Now we move to the double-dressed state. Among several known ways to doubly dress a spin qubit system [7~10], we choose the double dressing method using a secondary rf driving along the  $z$  axis. The bare qubit Hamiltonian is written as,

$$H \approx \frac{\omega_q}{2} \sigma_z + \sigma_z \sum_{\vec{r}} \left[ \frac{A_{\parallel\vec{r}}}{2} I_{z,\vec{r}} + \frac{A_{\perp\vec{r}}}{2} I_{x,\vec{r}} \right] + \sum_{\vec{r}} \gamma_{n,\vec{r}} B I_{z,\vec{r}} + \epsilon \sigma_z + \Omega_{\text{MW}} \cos(\omega_{\text{MW}} t) \sigma_x +$$

$$\Omega_{\text{RF}} \cos(\omega_{\text{RF}}t) \sigma_z. \quad (\text{S7})$$

Compared to eq. S2, we now have two driving terms, i.e. microwave and rf. Again for simplicity we drive the microwave field resonantly ( $\delta_{\text{MW}} \approx 0$ ). Then the single-dressed Hamiltonian becomes

$$H_{\text{SD}} \approx \frac{\Omega_{\text{MW}}}{2} \sigma_x + \sum_{\vec{r}} \left[ \frac{A_{\parallel, \vec{r}}}{2} \sigma_z I_{z, \vec{r}} + \frac{A_{\perp, \vec{r}}}{2} \sigma_z I_{x, \vec{r}} \right] + \sum_{\vec{r}} \gamma_{n, \vec{r}} B I_{z, \vec{r}} + \epsilon \sigma_z + \Omega_{\text{RF}} \cos(\omega_{\text{RF}}t) \sigma_z. \quad (\text{S8})$$

If we change the frame to be on the new eigenbasis,

$$\tilde{H}_{\text{SD}} \approx \frac{\Omega_{\text{MW}}}{2} \tilde{\sigma}_z + \Omega_{\text{RF}} \cos(\omega_{\text{RF}}t) \tilde{\sigma}_x + \sum_{\vec{r}} \left[ \frac{A_{\parallel, \vec{r}}}{2} \tilde{\sigma}_x I_{z, \vec{r}} + \frac{A_{\perp, \vec{r}}}{2} \tilde{\sigma}_x I_{x, \vec{r}} \right] + \sum_{\vec{r}} \gamma_{n, \vec{r}} B I_{z, \vec{r}} + \epsilon \tilde{\sigma}_x \quad (\text{S9})$$

, where  $\tilde{\sigma}_z = \sigma_x$  and  $\tilde{\sigma}_x = \sigma_z$ . The two leading terms in eq. S9 looks just the same as a bare qubit with a driving field. We now move to the new rotating frame, which is the double-dressed frame.

$$H_{\text{DD}} \approx \frac{\delta_{\text{RF}}}{2} \tilde{\sigma}_z + \frac{\Omega_{\text{RF}}}{2} \tilde{\sigma}_x + \sum_{\vec{r}} e^{i\frac{\omega_{\text{RF}}}{2}t\tilde{\sigma}_z} \tilde{\sigma}_x e^{-i\frac{\omega_{\text{RF}}}{2}t\tilde{\sigma}_z} \left[ \frac{A_{\parallel, \vec{r}}}{2} I_{z, \vec{r}} + \frac{A_{\perp, \vec{r}}}{2} I_{x, \vec{r}} \right] + \epsilon e^{i\frac{\omega_{\text{RF}}}{2}t\tilde{\sigma}_z} \tilde{\sigma}_x e^{-i\frac{\omega_{\text{RF}}}{2}t\tilde{\sigma}_z} + \sum_{\vec{r}} [\gamma_{n, \vec{r}} B I_{z, \vec{r}}] \quad (\text{S10})$$

, where  $\delta_{\text{RF}} = \Omega_{\text{MW}} - \omega_{\text{RF}}$ . If we assume the second drive is also on resonance,  $\delta_{\text{RF}} = 0$  and change the frame to be on the new double-dressed basis, the Hamiltonian becomes,

$$H_{\text{DD}} \approx \frac{\Omega_{\text{RF}}}{2} \sigma_z + \sum_{\vec{r}} e^{i\frac{\omega_{\text{RF}}}{2}t\tilde{\sigma}_z} \tilde{\sigma}_x e^{-i\frac{\omega_{\text{RF}}}{2}t\tilde{\sigma}_z} \left[ \frac{A_{\parallel, \vec{r}}}{2} I_{z, \vec{r}} + \frac{A_{\perp, \vec{r}}}{2} I_{x, \vec{r}} \right] + \epsilon e^{i\frac{\omega_{\text{RF}}}{2}t\tilde{\sigma}_z} \tilde{\sigma}_x e^{-i\frac{\omega_{\text{RF}}}{2}t\tilde{\sigma}_z} + \sum_{\vec{r}} \gamma_{n, \vec{r}} B I_{z, \vec{r}} \quad (\text{S11})$$

, whose quantization axis is back to the  $z$  axis as same as the bare qubit. The nuclear spin Zeeman terms, or the NMR signals, survive throughout the transformations as they commute with the unitary transforms we apply. The hyperfine interaction and the energy fluctuation terms are further removed by RWA and the Hamiltonian finally becomes,

$$H_{\text{DD}} \approx \frac{\Omega_{\text{RF}}}{2} \sigma_z + \sum_{\vec{r}} \gamma_{n, \vec{r}} B I_{z, \vec{r}}. \quad (\text{S12})$$

In this regime, the double dressing once more decouples the qubit from the noisy spin bath and the environmental fluctuation. Note that through the hierarchy of the dressing procedure, the ratio of  $\omega_{\text{RF}}$  to  $\Omega_{\text{MW}}$  for the double-dressed qubit is smaller compared to the ratio of  $\omega_{\text{MW}}$  to  $\omega_q$  for the bare qubit. Although the approximation used to derive the Hamiltonians is still valid, there may exist non-zero higher order noise terms in the double-dressed Hamiltonian

making the spin qubit still vulnerable to the noisy environment.

## 8. Hamiltonian calculation based on spin 1 system

In the main text, we derive the qubit Hamiltonian based on the two-level system. Here we show the Hamiltonian calculation based on the  $S = 1$  spin system and consider an effective two-level system. The Hamiltonian for the single dressing case is written as, (we treat  $\hbar = 1$ )

$$H = DS_z^2 + \gamma_e BS_z + \Omega \cos(\omega t) S_x \quad (\text{S13})$$

, where  $D$  is the zero-field splitting,  $B$  is the applied magnetic field,  $\gamma_e$  is the gyromagnetic ratio of the electron spin and  $S$  ( $S_x, S_y, S_z$ ) is the spin 1 operator. The Hamiltonian can be expressed in the matrix form based on the basis  $\{|+1\rangle, |0\rangle, |-1\rangle\}$  as,

$$\begin{bmatrix} D + \gamma_e B & \frac{1}{\sqrt{2}} \Omega \cos(\omega t) & 0 \\ \frac{1}{\sqrt{2}} \Omega \cos(\omega t) & 0 & \frac{1}{\sqrt{2}} \Omega \cos(\omega t) \\ 0 & \frac{1}{\sqrt{2}} \Omega \cos(\omega t) & D - \gamma_e B \end{bmatrix}. \quad (\text{S14})$$

We move to the rotating frame via a unitary transform,

$$\hat{U} = e^{i\omega t S_z^2}. \quad (\text{S15})$$

Note that we use  $S_z^2$  in the exponent of the operator as the large zero field splitting is dominant in the Hamiltonian. Then the Hamiltonian becomes,

$$\begin{bmatrix} D + \gamma_e B - \omega & \frac{\Omega}{2\sqrt{2}} & 0 \\ \frac{\Omega}{2\sqrt{2}} & 0 & \frac{\Omega}{2\sqrt{2}} \\ 0 & \frac{\Omega}{2\sqrt{2}} & D - \gamma_e B - \omega \end{bmatrix} \quad (\text{S15})$$

, where  $\delta = D + \gamma_e B - \omega$ . If we tune the frequency of the driving field to the  $|0\rangle \leftrightarrow |-1\rangle$  transition, so that  $|+1\rangle$  state is far detuned by several GHz, we can ignore it and treat the system as an effective two-level system. For simplicity, we shift the energy level by  $-\delta/2$  so that the reduced two-level Hamiltonian becomes,

$$\frac{1}{2} \begin{bmatrix} -\delta & \frac{\Omega}{\sqrt{2}} \\ \frac{\Omega}{\sqrt{2}} & \delta \end{bmatrix}. \quad (\text{S17})$$

Once we define  $\tan(\theta) = \left(\frac{\Omega}{\sqrt{2}}\right)/\delta$ , the single dressed basis becomes,

$$\begin{bmatrix} |-\rangle \\ |+\rangle \end{bmatrix} = \begin{bmatrix} \cos\left(\frac{\theta}{2}\right) & -\sin\left(\frac{\theta}{2}\right) \\ \sin\left(\frac{\theta}{2}\right) & \cos\left(\frac{\theta}{2}\right) \end{bmatrix} \begin{bmatrix} |0\rangle \\ | -1\rangle \end{bmatrix} \quad (\text{S18})$$

, which is the same results as eq. S5

## 9. Hyperfine splitting on the dressed basis

This section explains the spin 1 Hamiltonian with hyperfine interactions. Consider spin 1/2  $^{13}\text{C}$  and the secular approximation, the Hamiltonian reads,

$$H = DS_z^2 + \gamma_e BS_z + A_{||} S_z I_z + A_{\perp} S_z I_x + \gamma_n B I_z \quad (\text{S19})$$

, where  $A_{||}$  and  $A_{\perp}$  are the parallel and perpendicular hyperfine couplings, and  $\gamma_n$  is the nuclear Lamor frequency. As  $m_s = +1$  resonance is a few GHz away from the others, we will focus on only the  $m_s = 0$  and  $m_s = -1$  sub-spin systems as an effective qubit. When the driving field  $\Omega \cos(\omega t) S_x$  is added, the Hamiltonian becomes,

$$H = \begin{bmatrix} \frac{\gamma_n B}{2} & 0 & \frac{\Omega \cos(\omega t)}{\sqrt{2}} & 0 \\ 0 & -\frac{\gamma_n B}{2} & 0 & \frac{\Omega \cos(\omega t)}{\sqrt{2}} \\ \frac{\Omega \cos(\omega t)}{\sqrt{2}} & 0 & D - \gamma_e B + \frac{\gamma_n B - A_{||}}{2} & -\frac{A_{\perp}}{2} \\ 0 & \frac{\Omega \cos(\omega t)}{\sqrt{2}} & -\frac{A_{\perp}}{2} & D - \gamma_e B + \frac{A_{||} - \gamma_n B}{2} \end{bmatrix}. \quad (\text{S20})$$

We move to the interaction picture via a unitary transform  $\hat{U} = e^{i\omega t S_z^2} \otimes \hat{I}$  and, after RWA, the matrix becomes,

$$H_{\text{RWA}} = \begin{bmatrix} \frac{\gamma_n B}{2} & 0 & \frac{\Omega}{2\sqrt{2}} & 0 \\ 0 & -\frac{\gamma_n B}{2} & 0 & \frac{\Omega}{2\sqrt{2}} \\ \frac{\Omega}{2\sqrt{2}} & 0 & D - \gamma_e B - \omega + \frac{\gamma_n B - A_{||}}{2} & -\frac{A_{\perp}}{2} \\ 0 & \frac{\Omega}{2\sqrt{2}} & -\frac{A_{\perp}}{2} & D - \gamma_e B - \omega + \frac{A_{||} - \gamma_n B}{2} \end{bmatrix}. \quad (\text{S21})$$

Once we define  $\delta = D - \gamma_e B - \omega$ ,

$$H_{\text{RWA}} = \begin{bmatrix} \frac{\gamma_n B}{2} & 0 & \frac{\Omega}{2\sqrt{2}} & 0 \\ 0 & -\frac{\gamma_n B}{2} & 0 & \frac{\Omega}{2\sqrt{2}} \\ \frac{\Omega}{2\sqrt{2}} & 0 & \delta + \frac{\gamma_n B}{2} - \frac{A_{\parallel}}{2} & -\frac{A_{\perp}}{2} \\ 0 & \frac{\Omega}{2\sqrt{2}} & -\frac{A_{\perp}}{2} & \delta - \frac{\gamma_n B}{2} + \frac{A_{\parallel}}{2} \end{bmatrix}. \quad (\text{S22})$$

Numerical calculation of eq. S22 is shown in Fig. S8 which plots the relative ratio of the hyperfine splitting between the single-dressed qubit and the bare spin qubit as a function of  $A_{\parallel}$  and  $A_{\perp}$ . For most of the parameter range, the ratio is larger than one meaning the hyperfine splitting becomes smaller after the dressing.

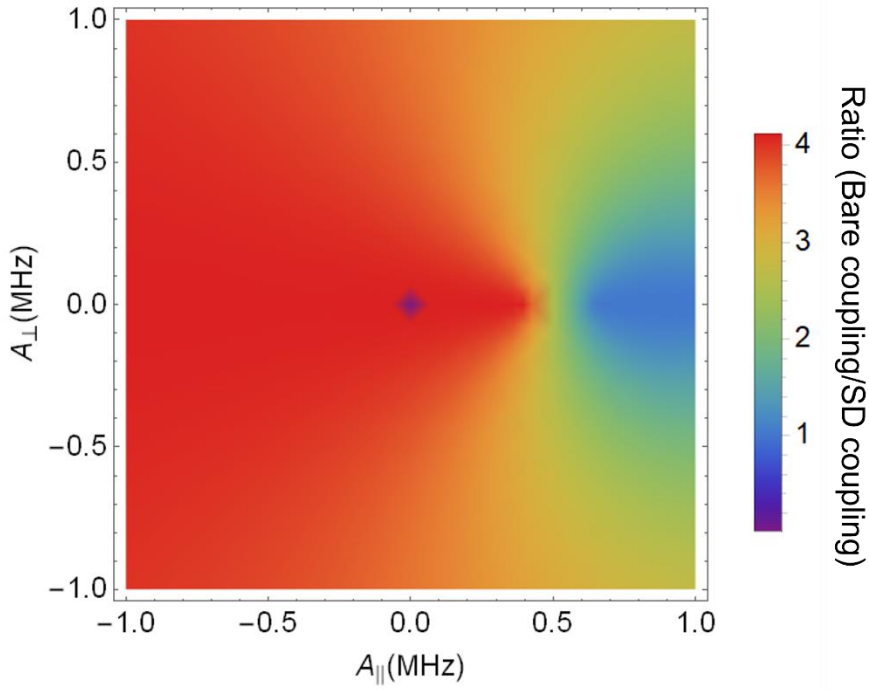


Fig. S8 Comparison of the hyperfine splitting between the bare spin qubit and the single-dressed qubit. We assume 405 G external field, 16 MHz Rabi frequency, and 4 MHz detuning. The minimum occurs around  $A_{\parallel} \sim 0.8 - 1.0$  MHz, where  $A_{\parallel}$  equals to  $2\gamma_n B$  i.e. twice of the  $^{13}\text{C}$  Larmor frequency at 405 G.

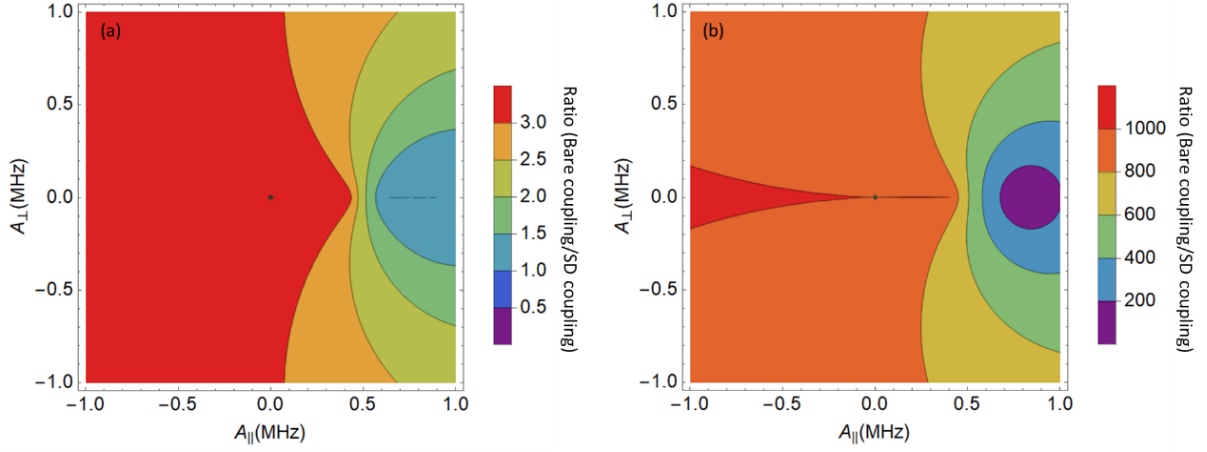


Fig. S9 Calculated hyperfine splitting with different detuning regimes. For better visualization, contour map is used. (a) 3 MHz detuning and 10 MHz Rabi frequency (b) 0.01 MHz detuning and 10 MHz Rabi frequency

In the main text, we assumed the “large detuning” regime for easier calculation of eq. S22 and derived the suppression factor of  $\frac{\delta_{\text{MW}}}{\sqrt{\delta_{\text{MW}}^2 + \Omega_{\text{MW}}^2}} \approx \frac{\delta_{\text{MW}}}{\Omega_{\text{MW}}}$ . This factor is valid for most of cases even including small detuning or resonance. Figure S9 shows numerical calculation of two different detuning regimes; large detuning and small detuning (nearly resonant). The red region in the contour plot of Fig. S9(a) indeed confirms that the ratio agrees well with the suppression factor of  $\frac{\delta_{\text{MW}}}{\Omega_{\text{MW}}}$ . Unless we are close to the minimum at  $A_{\parallel} \sim 0.8 - 1.0$  MHz, where  $A_{\parallel}$  cancels the effect of magnetic field,  $\gamma_n B$ , the factor is valid for most of the parameter space, especially near the zero point where most of the nuclear spin bath are responsible for. For the small detuning case in Fig. S9(b), the difference between the calculated ratio and the factor,  $\frac{\delta_{\text{MW}}}{\Omega_{\text{MW}}}$ , in the orange area is about 10-20 % and the discrepancy becomes larger for larger values of  $A_{\parallel}$  and  $A_{\perp}$ .

## 10. Calculations used in Fig. 4(a)

The hyperfine interaction transforms when the electron spin is dressed. When the electron spin is singly dressed, it is locked on the transvers plane and the nuclear spins experience a new

effective magnetic field including the hyperfine interaction,

$$\vec{B} - \frac{1}{2}(A_{\perp}, 0, A_{\parallel}) \quad (\text{S23})$$

, where  $\vec{B}$  is the static magnetic field in the lab frame [11]. Thus the new effective Larmor frequency of the nuclear spins becomes,

$$\sqrt{\left(\gamma_n B - \frac{A_{\parallel}}{2}\right)^2 + \left(\frac{A_{\perp}}{2}\right)^2}. \quad (\text{S24})$$

The frequencies of the six  $^{13}\text{C}$  nuclear spins in the upper graph of Fig. 4(a) are calculated from eq. S24 with randomly chosen values of  $A_{\parallel}$  and  $A_{\perp}$  from 0.1 MHz to 1.5 MHz. When the electron spin is doubly dressed as shown in the lower graph of Fig. 4(a), the hyperfine couplings in eq. S24 are reduced by a factor of  $\sim \frac{\delta_{\text{MW}}}{\omega_{\text{SD}}}$  and the peaks converge to the bare Larmor frequency of  $^{13}\text{C}$  nuclear spin at the given external field of  $\vec{B}$ .

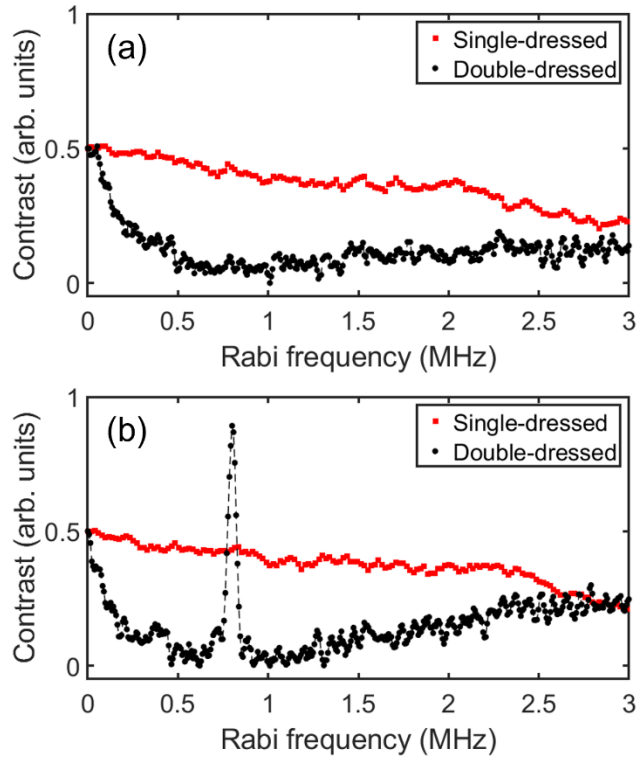


Fig. S10 Sub-MHz AC magnetometry. (a) With no applied signal, and (b) with a coherent AC signal at 0.8 MHz with 1.2  $\mu\text{T}$  amplitude. The signal is detected in the double-dressed measurement with  $\text{SNR} \approx 17$ .



## 11. AC sensing test with coherent signal

As discussed in Fig. 4(c), we test sub-MHz AC magnetometry with both stochastic and coherent signals. The former is already discussed in the main text, and here we show the result of the latter. Figure S10 shows before and after we introduce a coherent signal at 0.8 MHz with 1.2  $\mu\text{T}$  amplitude. While the signal is not observed in the single-dressed measurement, it is clearly visible in the double-dressed data with  $\text{SNR} \approx 17$ . Note that the small bump around 0.4 MHz may correspond to the  $^{13}\text{C}$  Larmor frequency in this measurement.

## 12. Note on vector AC magnetometry

We note that the sensing method described in Fig. 3 can provide a novel way to realize vector AC magnetometry in the rf frequency band. The single- and double-dressed qubits in Fig. 3(a) are nearly (if non-zero detuning) or perfectly (if resonantly driven) orthogonal to each other and they are sensitive to the AC field with either the longitudinal,  $\sigma_z$ , or the transverse,  $\sigma_x$ , components. Meanwhile, the qubit energy is tunable over the wide range of frequency mainly limited by the maximum applicable power of microwave and rf field. Therefore, as long as the RWA maintains through the hierarchy of the dressed state transitions, the method can be used for vector AC magnetometry in the wide range of rf frequency band. Not discussed in this paper, but it is also possible to control the phase of the driving field or to use amplitude modulated driving to lock the spin along the  $y$  axis [12] to obtain the  $\sigma_y$  component of the field. We also note that G. Wang *et al.* [13] recently demonstrated vector AC magnetometry of rf field using the spin locking technique. But it differs from our method as they applied large magnetic field e.g.  $\sim 1000$  G to match the resonance conditions for the longitudinal and transverse components of the rf field.

As an alternative way to realize vector AC magnetometry, one may implement mixed dynamical decoupling (MDD) that combines CDD and PDD [14]. For instance, the double dressing method can be implemented together with PDD such as Hahn echo. Hahn echo pulse sequence typically picks up the component parallel to the principal axis of the sensor spin. As we can tilt the principal axis of the single- or double-dressed qubits by adjusting detuning and Rabi frequency, combination with Hahn echo can allow us to probe arbitrary vector component

of AC magnetic field. Vector AC magnetometry based on MDD could be an interesting topic for the future research.

#### References for supplemental material

- [1] J. Kölbl, A. Barfuss, M. S. Kasperczyk, L. Thiel, A. A. Clerk, H. Ribeiro, and P. Maletinsky, Initialization of single spin dressed states using shortcuts to adiabaticity, *Phys. Rev. Lett.* 122, 090502 (2019).
- [2] M. Demirplak and S. A. Rice, Adiabatic population transfer with control fields, *J. Phys. Chem. A* 107, 9937 (2003).
- [3] D. Guéry-Odelin, A. Ruschhaupt, A. Kiely, E. Torrontegui, S. Martínez-Garaot, and J. Muga, Shortcuts to adiabaticity: Concepts, methods, and applications, *Rev. Mod. Phys.* 91, 045001 (2019).
- [4] K. N. Zlatanov, and N. V. Vitanov, Adiabatic generation of arbitrary coherent superpositions of two quantum states: Exact and approximate solutions, *Phys. Rev. A* 96, 013415 (2017)
- [5] J. R. Johansson, P. D. Nation, and F. Nori: "QuTiP 2: A Python framework for the dynamics of open quantum systems.", *Comp. Phys. Comm.* 184, 1234 (2013)
- [6] J. R. Johansson, P. D. Nation, and F. Nori: "QuTiP: An open-source Python framework for the dynamics of open quantum systems.", *Comp. Phys. Comm.* 183, 1760–1772 (2012)
- [7] V. Jacques, P. Neumann, J. Beck, M. Markham, D. Twitchen, J. Meijer, F. Kaiser, G. Balasubramanian, F. Jelezko, and J. Wrachtrup, Dynamic polarization of single nuclear spins by optical pumping of nitrogen vacancy color centers in diamond at room temperature, *Phys. Rev. Lett.* 102, 057403 (2009).
- [8] I. Cohen, S. Weidt, W. K. Hensinger, and A. Retzker, Multi-qubit gate with trapped ions for microwave and laser-based implementation, *New J. Phys.* 17, 043008 (2015).
- [9] J.-M. Cai, B. Naydenov, R. Pfeiffer, L. P. McGuinness, K. D. Jahnke, F. Jelezko, M. B. Plenio, and A. Retzker, Robust dynamical decoupling with concatenated continuous driving, *New J. Phys.* 14, 113023 (2012).

- [10] A. Laucht, R. Kalra, S. Simmons, J. P. Dehollain, J. T. Muhonen, F. A. Mohiyaddin, S. Freer, F. E. Hudson, K. M. Itoh, D. N. Jamieson, J. C. McCallum, A. S. Dzurak, and A. Morello, A dressed spin qubit in silicon, *Nat. Nanotechnol.* 12, 61 (2017).
- [11] P. London, J. Scheuer, J.-M. Cai, I. Schwarz, A. Retzker, M. B. Plenio, M. Katagiri, T. Teraji, S. Koizumi, J. Isoya, R. Fischer, L. P. McGuinness, B. Naydenov, and F. Jelezko, *Phys. Rev. Lett.* 111, 067601 (2013)
- [12] A. Stark, N. Aharon, T. Uden, D. Louzon, A. Huck, A. Retzker, U. L. Andersen, and F. Jelezko, Narrow-bandwidth sensing of high-frequency fields with continuous dynamical decoupling, *Nat. Commun.* 8, 1105 (2017).
- [13] G. Wang, Y.-X. Liu, Y. Zhu, and P. Cappellaro, Nanoscale Vector AC Magnetometry with a Single Nitrogen-Vacancy Center in Diamond, *Nano Lett.* 21, 5143–5150 (2021).
- [14] G. T. Genov, N. Aharon, F. Jelezko and A. Retzker, Mixed dynamical decoupling, *Quantum Sci. Technol.* 4 035010 (2019).